Post-2018 caldera collapse re-inflation uniquely constrains Kīlauea's magmatic system

Taiyi Wang [1], Yujie Zheng [2], Fabio Pulvirenti [3], Paul Segall [1]

[1]Department of Geophysics, Stanford University
[2]Division of Geological and Planetary Sciences, California Institute of Technology
[3]Jet Propulsion Laboratory, California Institute of Technology

Key Points:

- Simultaneous summit inflation and deflation constrains the location and geometry of Halema'uma'u (HMM) and South Caldera (SC) reservoirs.
- A model with time dependent magma flux between reservoirs explains the post-collapse spatial-temporal deformation pattern.
- Time dependent deformations require a HMM-East Rift Zone (ERZ) pathway and possibly a less hydraulically conductive SC-ERZ pathway.

Corresponding author: Taiyi Wang, `taiyi@stanford.edu`

1 Abstract

From August 2018 to May 2019, Kīlauea's summit exhibited unique, simultaneous, inflation and deflation, apparent in both GPS time series and Small Baseline Subset (SBAS) derived cumulative InSAR displacement maps. This deformation pattern provides clear evidence that Halemaʻumaʻu (HMM) and South Caldera (SC) are distinct reservoirs. Post-collapse inflation of the East Rift Zone (ERZ), as captured by InSAR, indicates concurrent magma transfer from the summit reservoirs to the ERZ. We present a physics-based model that couples pressure-driven flow between magma reservoirs to simulate time dependent summit deformation. We take a two-step approach to quantitatively constrain Kīlauea's magmatic plumbing system. First, we jointly invert the cumulative displacement maps and GPS offsets for the location and geometry of the summit reservoirs, approximated as spheroidal chambers. We find that HMM reservoir has an aspect ratio of ~ 1.8 (prolate) and a depth of ~ 2.2 km (below surface). The SC reservoir has an aspect ratio of ~ 0.15 (oblate) and a depth of ~ 3.6 km. Second, we utilize the flux model to invert GPS time series from 8 summit stations. Results favor a shallow HMM-ERZ pathway an order of magnitude more hydraulically conductive than the deep SC-ERZ pathway. Further experiments indicate that the HMM-ERZ pathway is required to explain the deformation time series. Given high-quality geodetic data, such an approach promises to quantify the connectivity of magmatic pathways between reservoirs in other similar volcanic systems.

2 Introduction

The supply, storage, and subsurface transport of magma are some of the most fundamental, yet least understood volcanic processes (Poland et al., 2014). These processes, along with eruptive dynamics, are modulated by the geometry and nature of the pathways connecting magmatic reservoirs (Keating et al., 2008). The geometry and dimensions of individual pathways can be constrained by inverting surface deformation with continuum mechanics based models (e.g. Owen et al., 2000; Montagna & Gonnermann, 2013). However, in the presence of multiple reservoirs and a network of magmatic pathways, estimating the dimensions of each pathway directly from deformation can be challenging. Because magma flux is proportional to the hydraulic conductivity of the pathway, and pressure change in a reservoir depends on magma flux, time dependent deformation associated with each reservoir may reveal the connectivity of a multi-reservoir system (e.g. Reverso et al., 2014; Bato et al., 2018). Here we demonstrate that, physics-based models, coupled with Bayesian inversion, can synthesize multi-reservoir conceptual models with geodetic measurements to quantitatively constrain the hydraulic connectivity of magmatic systems.

Despite decades of research, the nature of Kīlauea's summit reservoirs and their connectivity to the ERZ remains enigmatic. Efforts to interpret observed deformation in terms of simple reservoir models yielded different reservoir locations and geometries (e.g. Fiske & Kinoshita, 1969; Baker & Amelung, 2012). Although modeled reservoirs cluster into two groups - a shallow Halemaʻumaʻu (HMM) and a deeper South Caldera (SC) reservoir (e.g. Cervelli & Miklius, 2003; Poland et al., 2014), it has been suggested that the summit system represents a single irregularly shaped reservoir (Dieterich & Decker, 1975; Ryan, 1988). This ambiguity arises because deformation signals associated with these reservoirs are of the same sign. The nature of the connection between Kīlauea's summit and the ERZ is also elusive. Cervelli and Miklius (2003) argue that an "L" shaped connection from SC to ERZ via HMM is required to explain the drainage of excess magma from HMM during the deflationary stage of Deflation-Inflation events. Poland et al. (2014) suggest that the ERZ is connected to the summit directly via the SC, which is informed by depths of seismicity associated with ERZ dike intrusions. Therefore, a robust constraint on the location and geometry of the summit reservoirs, as well as quantitative estimates on the conductivity of magma pathways address these unresolved questions.

We report here on post caldera collapse simultaneous inflationary and deflationary deformation northeast and southeast of the caldera, respectively. During this period, there was concurrent inflationary deformation in the section of ERZ near Puu Ōō. These observations suggest a volume increase in the inferred HMM reservoir, a volume decrease in the inferred SC reservoir, and a volume increase in the ERZ, providing an unprecedented opportunity to elucidate the nature of Kīlauea's magmatic plumbing system (Fig. 1). GPS stations in the summit region registered continued deflation (Fig. 2) after eruption ended in August 2018. By October 2018, GPS stations on the northwestern side of the caldera (e.g. UWEV) started to register inflation, while stations on the southeastern side of the caldera (e.g. PUHI) experienced continued deflation (Fig. 2). By mid-May 2019, all of the GPS stations in the summit area exhibited a gradual inflationary signal (Fig. 2). The delayed inflation from the southeastern side of the caldera suggests that SC supplied magma to the ERZ and HMM. Modeling the spatial-temporal summit deformation could lead to quantitative constraints not only on the location and geometry of the summit reservoirs, but also the connectivity of magmatic pathways between the summit magma system and the ERZ.

We present our findings in the following order: in section 3, we introduce the relevant GPS and InSAR data sets. Details on data analyses and covariance matrices can be found in Appendices A and B. We then perform a "static" inversion, where GPS offsets and Line of Sight (LoS) cumulative displacement maps are used to estimate the location and geometry of the HMM and SC reservoirs (Section 4). Because approximate, semi-analytical, spheroidal source models are used in this inversion, we examine their accuracy by comparing predicted surface deformation with that of a 3D finite element model, given the same set of model parameters. In addition, we perform an inversion with the finite element model to ensure that the estimated parameters are not biased by limitations of the semi-analytical model. In section 4, we also estimate the aspect ratio and depth of the ERZ reservoir by inverting InSAR LoS displacements. In section 5, we introduce a model to relate flux-controlled reservoir pressure with time dependent surface deformation. Finally, we perform a "dynamic" inversion using GPS time series to estimate the effective hydraulic conductivity of various pathways in Kīlauea's magmatic plumbing system. In section 7, we discuss the implications of the inversion results.

3 Geodetic data

3.1 Global Positioning System (GPS)

Three-component, daily GPS solutions were retrieved for the period between Aug. 9, 2018 and Dec. 1, 2019 from 8 USGS operated GPS stations at Kīlauea's summit. We do not correct for south flank motion or potential deformation of Mauna Loa. In the vicinity of the caldera, long term south flank motion is relatively small (up to a couple of centimeters per year in the horizontal component at AHUP (Poland et al., 2017)) compared to the summit deformation signals. Mauna Loa did not exhibit significant deformation over the study period. Detailed discussion of the noise covariance matrix of GPS time series data can be found in Appendix A.

3.2 Interferometric Synthetic Aperture Radar (InSAR)

We utilize InSAR data to gain better spatial constraints on post-collapse deformation. For the summit area, we retrieved 44 ascending (path 124, frame 55-60) and 48 descending (path 524-529, frame 76) Sentinel-1 scenes from Alaska Satellite Facility's data repository. Acquisitions were processed using a geocoded SAR processor (Zebker, 2017; Zheng & Zebker, 2017). Acquisitions span the period from Aug. 6, 2018 to May 27, 2019. To increase the signal to noise ratio, we perform a Small Baseline Subset (SBAS) time series analysis (Berardino et al., 2002). The SBAS derived time series displacements (Fig. B1) for each pixel are used to compute cumulative displacement maps in the Line of Sight

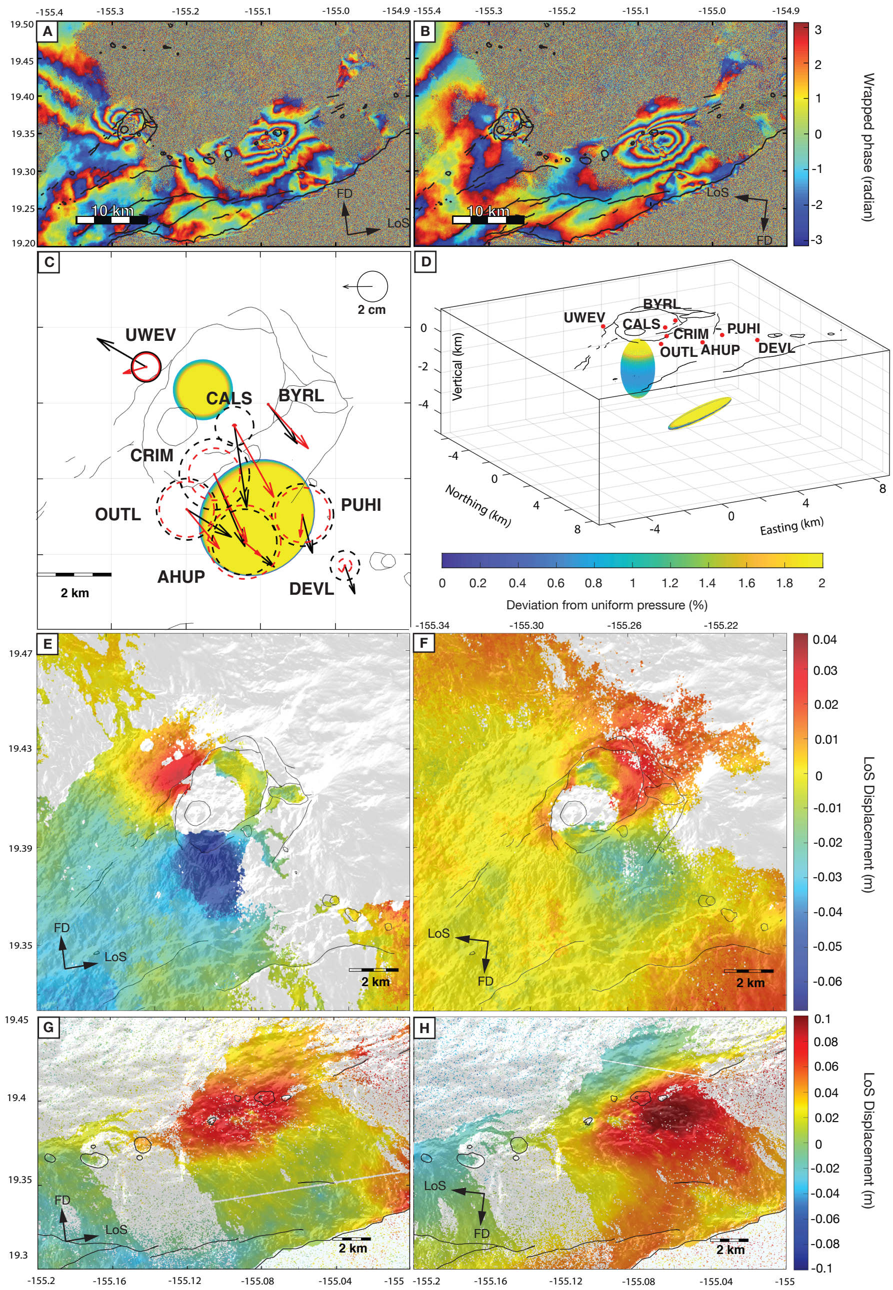

Figure 1: Post-collapse deformation at Kīlauea. (a), (b) : ascending (Nov. 22, 2018 - May 27, 2019) and descending (Nov. 13, 2018 - May 30, 2019) wrapped interferograms of the summit region and the ERZ. Each fringe (blue-yellow-red) corresponds to 28 mm of displacement towards the satellite. (c): Comparison of GPS displacement with predictions from the best-fit model. Arrows and circles indicate radial and vertical displacements, respectively. Data is in black and predictions in red. Downward vertical displacement is in dashed circles. Also included is the map view of the two best-fit spheroidal source models from the static inversion. The spheroid to the NW represents the HMM reservoir; the spheroid to the SE represents the SC reservoir. (d): Perspective view of the best fit spheroid models. Color bar indicates the deviation from the uniform pressure boundary condition for a spheroidal cavity in an elastic half space. (e), (f): SBAS derived ascending (Nov. 4, 2018 - Mar. 16, 2019) and descending (Nov. 1, 2018 - Mar. 19, 2019) cumulative displacement maps, respectively. Areas with low coherence or large phase unwrapping errors are masked out. Color bar indicates range change in meters, with positive numbers indicating decreasing distance between satellite and ground. Black lines overlying the DEM demarcate the outline of the caldera prior to 2018 collapse. (g), (h): ascending (Nov 4, 2018 - Mar. 16, 2019) and descending (Nov 1, 2018 - Mar. 19, 2019) LoS displacements of the ERZ derived from interferograms, respectively.

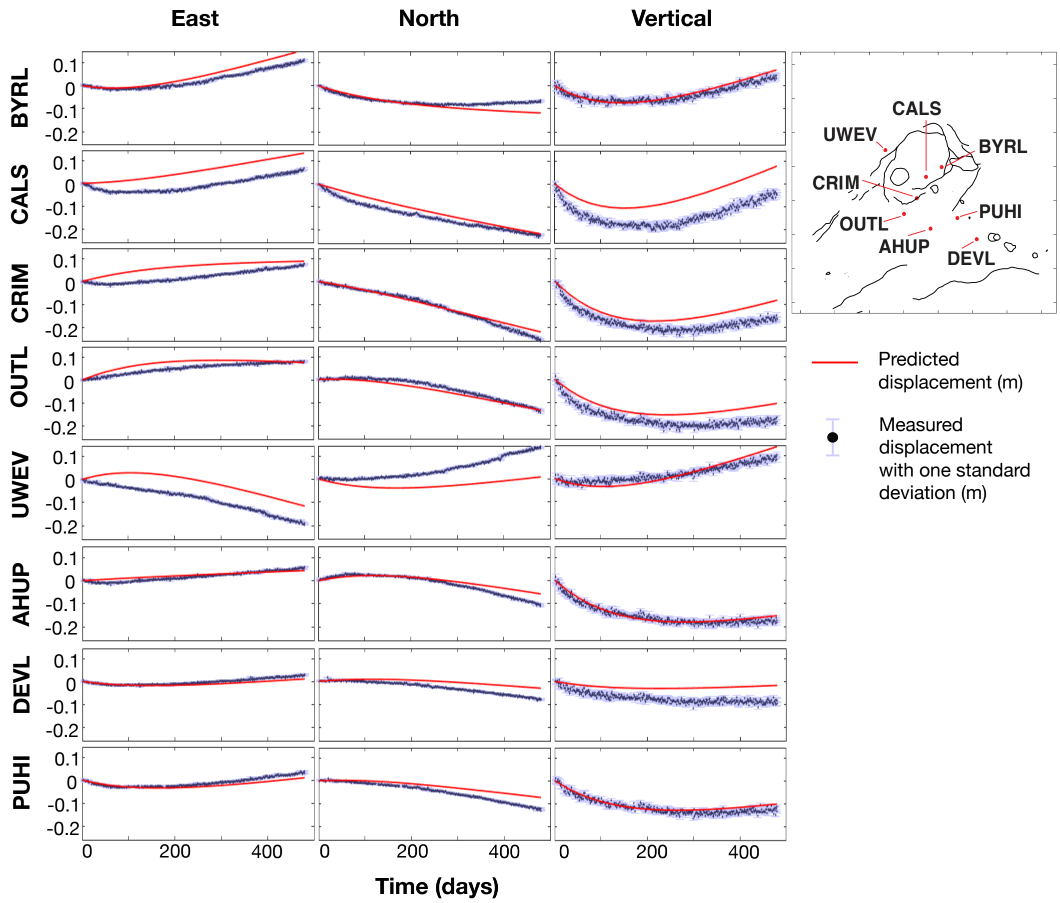

Figure 2: Summit GPS time series and model predictions. Error bars are ±1 standard deviation. Inset: station locations relative to the caldera.

(LoS) directions (Fig. 1 e, f). Detailed procedures on SBAS and noise covariance matrices are in Appendix B. For the ERZ, we formed 2 interferograms from 2 ascending acquisitions (Nov. 4, 2018 - Mar. 16, 2019) and 2 descending acquisitions (Nov. 1, 2018 - Mar. 19, 2019) from Sentinel-1.

4 Static inversion for the geometry and location of reservoirs

4.1 Summit reservoirs

4.1.1 Bayesian inversion using the Yang-Cervelli model

We use GPS offsets and SBAS derived cumulative displacement maps to estimate the parameters that describe the HMM and SC reservoirs' horizontal location, depth, aspect ratio and orientation. A semi-analytical, approximate model originally proposed by Yang et al. (1988) to compute surface displacements due to a pressurized prolate spheroidal cavity, later extended by Cervelli (2013) to include oblate cavities, is used to relate pressure change to surface displacements. We refer to this as the Yang-Cervelli model. We first invert the cumulative displacements and thus refer to it the "static inversion". We employ a Bayesian framework to estimate posterior probability density function (PDF) of the model parameters:

$$P(\boldsymbol{m}|\boldsymbol{d}) \propto P(\boldsymbol{d}|\boldsymbol{m})P(\boldsymbol{m}) \tag{1}$$

where $\boldsymbol{m}$ denotes model parameters and $\boldsymbol{d}$ the data. Eqn. 1 states that the probability of a model conditioned on data, $P(\boldsymbol{m}|\boldsymbol{d})$ (posterior), is proportional to the product of the likelihood, $P(\boldsymbol{d}|\boldsymbol{m})$, and the prior distribution of the model parameters, $P(\boldsymbol{m})$. In practice, the posterior PDF is estimated by a Markov Chain Monte Carlo (MCMC) procedure. We assume the data errors are normally distributed, such that:

$$P(\boldsymbol{d}|\boldsymbol{m}) = (2\pi)^{-N/2}det(\boldsymbol{C})^{-1/2} \times exp[-\frac{1}{2}(\boldsymbol{d}-\boldsymbol{G}(\boldsymbol{m}))^T\boldsymbol{C}^{-1}(\boldsymbol{d}-\boldsymbol{G}(\boldsymbol{m}))] \tag{2}$$

Here, N is the number of data, $\boldsymbol{C}$ is the data covariance matrix, $\boldsymbol{G}$ is the forward model operator. The accuracy of Eqn. 2 is predicated on having the correct covariance matrices for each data set. Three-component GPS offsets (Fig. 1 c) and SBAS-derived, quadtree down-sampled LoS cumulative displacement maps (Fig. 4 a, d) are used in the inversion.

To account for the disparity in the number of data points among GPS and InSAR data sets, we weighted the log likelihood of GPS data by a factor of 1000. This was obtained by inverting for the best-fit model with weight factors between 1 and 1500, and computing the residuals to both the GPS and InSAR data. With a weight factor of 1000 (Fig. C1), the prediction minimizes the L2 norm of covariance weighted residuals to each data set without compromising goodness-of-fit for either (Simons et al., 2002).

We use Gaussian-tailed uniform distributions for the priors (Anderson & Poland, 2016), where the standard deviation of the tail is 10% the width of the uniform part. The choice of the prior, $P(\boldsymbol{m})$, is informed by previous studies at Kīlauea. We use the approximate range of Anderson et al. (2019)'s posterior distribution as priors for the horizontal location, depth, and aspect ratios for HMM (Table 1). Preliminary inversions indicate that prior constraints on the N-S location, depth, and aspect ratio of HMM may be overly restrictive for the post-collapse period. In particular, the inverted aspect ratio was consistently higher than the 0.8-1.4 range found by Anderson et al. (2019). Due to the caldera collapse and the slumping of crustal material into the reservoir, it is plausible that the geometry of the hydraulically active part of the HMM reservoir evolved over time. To allow for complete sampling of the model space, we extend the upper bounds on the N-S location, depth, and aspect ratio of HMM for the final inversion. We use previously inferred locations associated with SC as bounds on the prior (Baker & Amelung, 2012; Poland et al., 2014). The inferred SC volume generally falls between 2 and 20 km^3 (Poland et al., 2014). As expected, the goodness of fit is not sensitive to the volume of

parameter	symbol	units	bounds on prior	MAP model	90% confidence interval
HMM E-W location	Δx_{HMM}	km	[0.3 0.5] [1]	0.46	[0.35 0.45]
HMM N-S location	Δy_{HMM}	km	[0.2 0.5] [1]	0.35	[0.30 0.41]
HMM centroid depth	d_{HMM}	km	[-1.5 -2.2] [1]	-2.18	[-2.13 -2.19]
HMM aspect ratio	α_{HMM}	unit-less	[0.8 1.4] [1]	1.78	[1.70 1.79]
HMM pressure change	Δp_{HMM}	MPa	[1.5 2]	1.55	[1.53 1.62]
HMM volume	V_1	km^3	3.9 [1]	Fixed	
SC E-W location	Δx_{SC}	km	[-2.5 2.5] [2]	1.89	[1.78 1.95]
SC N-S location	Δy_{SC}	km	[-3.4 -1] [2]	-3.03	[-3.09 -2.91]
SC depth	d_{SC}	km	[-4.7 -2.7] [3]	-3.63	[-3.86 -3.52]
SC volume	V_2	km^3	2.5 [4]	Fixed	
SC aspect ratio	α_{SC}	unit-less	[0.1 1]	0.14	[0.12 0.21]
SC pressure change	Δp_{SC}	MPa	[-1.99 -0.001]	-0.88	[-1.38 -0.76]
SC dip	ϕ_{SC}	unit-less	[45 90]	63	[61 65]
SC strike	ψ_{SC}	unit-less	[0 360]	136	[128 141]

[1] Anderson et al., 2019; approximate posterior range
[2] Poland et al., 2014; approximate locations of distributed sill opening
[3] Baker and Amelung, 2012; 95% confidence interval for the depth of "source 3"
[4] Pietruszka and Garcia, 1999; magma mixing volume of SC inferred from residence time analysis

Table 1: Static inversion parameters, bounds on prior, MAP model, and 90% confidence interval. Horizontal locations are referenced to GPS station NPIT. The RMS misfit for the MAP model is 1.1 cm.

SC due to its trade off with pressure changes. Therefore, we use the estimated volume of 2.5 km^3 from Pietruszka and Garcia (1998) to compute the semi-major and -minor axes lengths of the SC.

Deformation data constrain the model parameters quite well (Fig. 3). For HMM, the best-fit values of Δx_{HMM} and Δy_{HMM} are well within its prior bounds. The best fit values of d_{HMM} and α_{HMM}, however, are close to their respective upper bounds. To honor the prior constraints on d_{HMM} and α_{HMM} established by previous studies (e.g. Anderson et al., 2019), we do not further extend the bounds on these parameters. The posterior distributions of SC's parameters are well resolved within the prior bounds. The best-fit aspect ratio of SC is ~ 0.18, which is close to its lower bound and indicates a sill-like body. This is consistent with previous studies that modeled the SC reservoir as a penny-shaped crack (Baker & Amelung, 2012) or with distributed crack opening (Poland et al., 2014). Because the inversion allows SC to deviate from a vertical orientation, we observe that, in the maximum a posteriori (MAP) model, the semi-major axis dips $\sim 65°$ towards the SSW; the posterior PDF of dip excludes a vertical orientation of the reservoir. The dip is a result of fitting the imbalanced eastward and westward displacements associated with SC deflation (Fig. 5). This feature is discussed further in Section 7.1.

The inflation northwest of the caldera and the deflation southeast of the caldera are well captured by the prediction of the MAP model (Fig. 1 c, d; Fig. 4). The RMS misfit for the combined GPS and InSAR measurements is 1.1 cm. Notable misfits in GPS include the radial displacement at UWEV and the vertical displacement at CALS. Because CALS is situated on the 2018 collapse block, the assumption of homogeneous elastic half space may be violated. The MAP model also under-predicts the ascending LoS range decrease and over-predicts the descending LoS range increase (Fig. 4). It is likely that spheroid source models can not capture the geometrical complexity of real magma

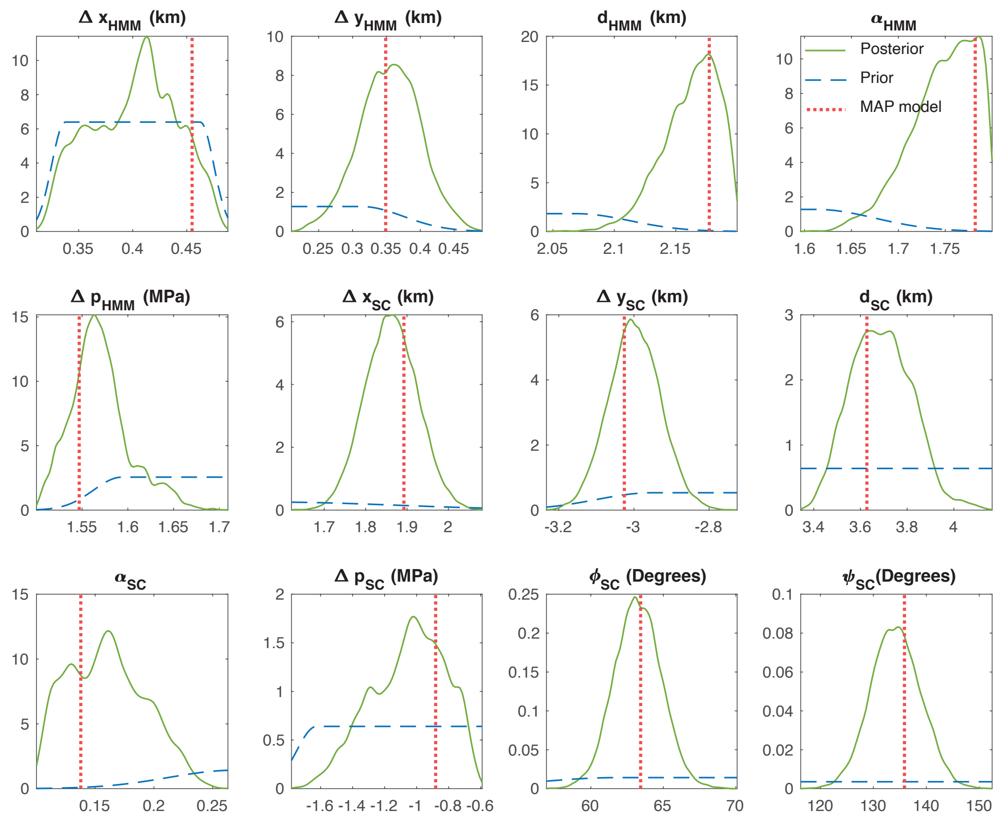

Figure 3: Posterior PDFs from static inversion after 1×10^5 MCMC iterations. Prior distributions are in blue dashed line; posterior distributions are in green; MAP model is in red dotted line. Gaussian tailed uniform distributions are used as priors, where the standard deviation of the tail is one tenth the width of the uniform part.

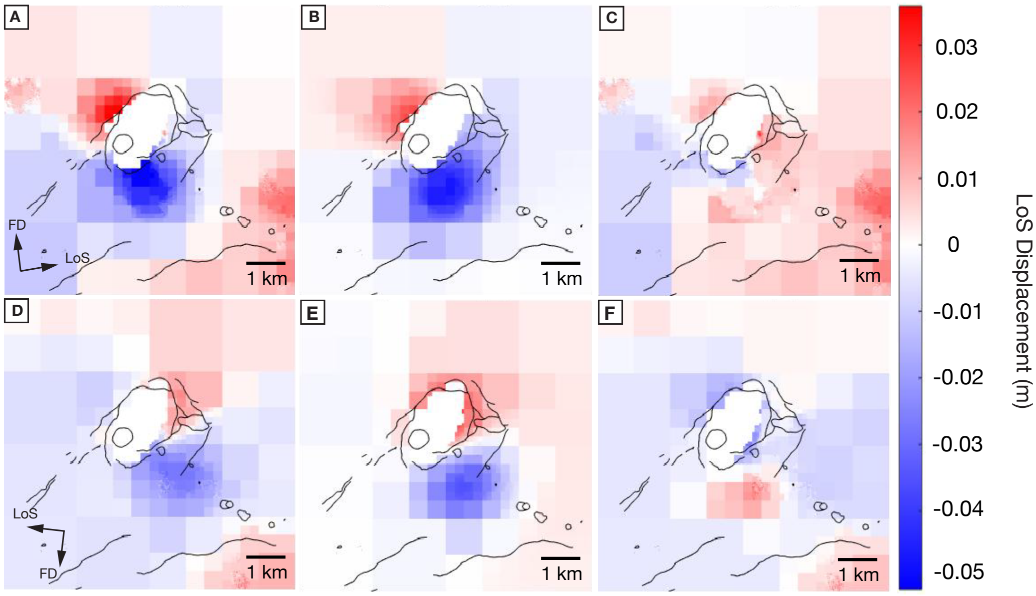

Figure 4: Quadtree down-sampled cumulative displacement maps, predictions from best fit model, and residuals. (a)-(c): cumulative displacement derived from ascending track interferograms, prediction from MAP model of the static inversion, and residuals. (d)-(e): cumulative displacement derived from descending track interferograms, prediction from MAP model of the static inversion, and residuals. Displacement in meters.

chambers. However, to ensure that the misfit is not due to approximations inherent in the Yang-Cervelli model, we input the MAP model from the static inversion into a finite element (FEM) model to compute more accurate predictions of surface deformation.

4.1.2 Comparison against FEM model prediction

Given a homogeneous elastic half space, the accuracy of using the Yang-Cervelli model to predict surface deformation hinges on two conditions: 1. the depth to effective radius ratio of the spheroid cavity is large, so that the boundary conditions at the cavity/solid boundary are reasonably satisfied; 2. elastic interactions between the two cavities are negligible. To test the accuracy of the Yang-Cervelli model, we construct a FEM model in COMSOL based on the MAP model from the static inversion. Mesh sensitivity tests are performed to ensure the adequacy of the mesh resolution. We compare the observed E-W and vertical displacements to the Yang-Cervelli predictions, and the FEM predictions (Fig. 5). Displacements in East-North-Up (ENU) are inverted from the LoS cumulative displacement maps (Fialko et al., 2001). The north component of displacement is negligible because the near east-west SAR viewing angle is not sensitive to north-south displacements.

The Yang-Cervelli MAP model under-predicts the westward displacement west of HMM by more than 1 cm (Fig. 5), whereas the FEM model under-predicts the westward displacement by a lesser degree. In the vertical component, the Yang-Cervelli model over-predicts the deflation to the southeast of the caldera, whereas the FEM model over-predicts both the inflation and the deflation. In both east and vertical components, the deformation pattern predicted by the FEM model is broader than predicted by the Yang-Cervelli model, which suggests that the depth of the HMM and SC reservoirs could be shallower than inferred from the Yang-Cervelli model. This raises the possibility that inversion with

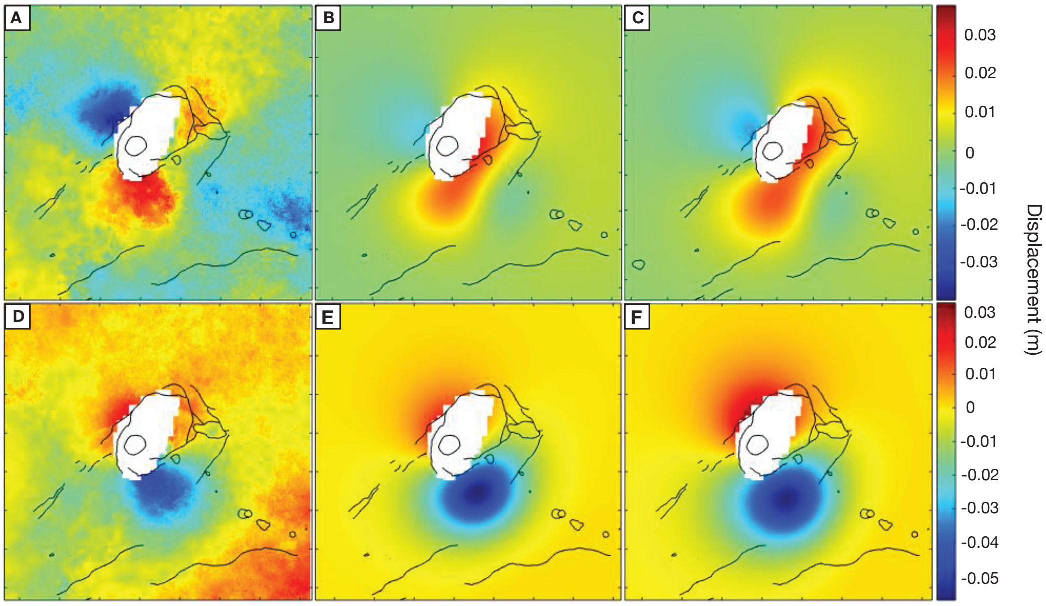

Figure 5: Comparison of SBAS derived cumulative displacement (between Nov. 4, 2018 and Mar. 16, 2019) with model predictions. (a)-(c): East component of measured deformation, prediction of MAP model, and prediction of MAP parameters as input into the FEM model, respectively. (d)-(e): vertical component of measured deformation, prediction of MAP model, and prediction of the FEM model with MAP parameters as input. Deformation within the caldera is masked due to potential unwrapping errors.

the FEM model could yield a more accurate location and geometry of the two reservoirs. In the next section, we demonstrate that inversion results from the Yang-Cervelli model is, in fact, not dissimilar to that from the more computationally expensive FEM model.

4.1.3 Nelder Mead inversion using a FEM model

To test the accuracy of inversion results from the Yang-Cervelli model, we perform an inversion with the FEM model and search within the $\sim \pm 2\sigma$ of the static inversion's posterior PDFs. We use the Nelder Mead method for the inversion. In doing so, we recognize that differences in inversion results could come from either the difference in inversion schemes (MCMC vs. Nelder Mead) or difference in forward model (Yang-Cervelli vs. FEM). In this section, we demonstrate that, differences in inversion methods do not influence inversion results appreciably, and using the FEM model in lieu of the Yang-Cervelli model has a small effect on the inverted parameters.

Due to COMSOL's inability to include a non-diagonal covariance matrix, we opt to use a reduced set of data for this inversion. The reduced data set is comprised of LoS displacements for 10 spatially separated InSAR pixel points and 3-component GPS offsets during the same period. The 10 pixel points are chosen based on the rationale that the spatial correlation of atmospheric noise decreases exponentially with distance. For the same forward model and inversion scheme, the inverted model parameters are insensitive to full vs. reduced data set (Appendix D).

We use the MAP model from the static inversion (MCMC + Yang-Cervelli) as the starting model, and run the Nelder Mead + FEM inversion for 100 iterations, upon which the objective function converged to a constant value. The normalized difference between the best fit model parameters of the Nelder Mead inversion and the MAP model param-

parameter	units	Generalized pattern search + Yang Cervelli	Nelder Mead + FEM
a_{HMM}	km	0.56	0.36
b_{HMM}	km	0.47	0.27
d_{HMM}	km	-2.1	-2.2
α_{HMM}	unit-less	1.9	1.7
Δp_{HMM}	MPa	1.6	1.4
a_{SC}	km	1.8	1.5
b_{SC}	km	-2.9	-3.1
d_{SC}	km	-3.5	-3.6
α_{SC}	unit-less	0.16	0.14
Δp_{SC}	MPa	-1.4	-0.88
ϕ_{SC}	unit-less	121	116
ψ_{SC}	unit-less	-48	-32

Table 2: Best fit models from generalized pattern search + Yang Cervelli (RMS misfit = 1.06 cm) and Nelder Mead + FEM (RMS misfit = 1.10 cm). Note that the inverted data set is LoS displacements from 10 pixels on the cumulative displacement maps and GPS offsets from 8 stations.

eters is $< 10\%$. Because Nelder Mead is a downhill simplex algorithm, the inversion results may be sensitive to the initial model. To ensure that Nelder Mead inversion searched extensively over the model space, we perform a separate inversion using a generalized pattern search algorithm (Audet & Dennis Jr, 2002) with the same bounds, and the Yang-Cervelli model. This inversion yields a best-fit model (Table 2) and a prediction (Fig. 6) very similar to those obtained by Nelder Mead + FEM. The generalized pattern search algorithm has been demonstrated to be able to search over multiple local minima (Audet & Dennis Jr, 2002). Therefore, the similarity between the model found by generalized pattern search + Yang-Cervelli and the model found by Nelder Mead + FEM demonstrates the robustness of the Nelder Mead inversion. The similarity of the inverted parameters from both Nelder Mead + FEM and generalized pattern search + Yang-Cervelli to those from the MAP model demonstrates that inversions using the approximate Yang-Cervelli model yields accurate results, as compared to those from the computationally expensive FEM model. This justifies our use of the Yang-Cervelli model for subsequent dynamic inversions (Section 6).

4.2 ERZ reservoir

Inflationary deformation in the ERZ provides important constraints on the geometry and depth of reservoir(s) in this region. In particular, the inverted depth range is used as prior information (Appendix E) for the dynamic inversion. Since the focus of this study is on summit deformation, we jointly invert the quadtree down-sampled ascending and descending interferograms at ERZ using surrogate optimization (Gutmann, 2001), instead of sampling the full PDFs using MCMC. A single Yang-Cervelli spheroid is used as the source model. We use the L2 norm of misfit weighed by spatial covariance matrices (obtained using the same method as detailed in Appendix B) as the objective function. The best fit model is a spheroid with an aspect ratio of 15.3, with a nearly horizontal semi-major axis striking sub-parallel to the East Rift Zone. The centroid is ~ 2.3 km below the surface. The aspect ratio and centroid depths are not sensitive to the input reservoir volume. For a hypothetical volume of 2.5×10^9 m^3, the semi-major axis is ~ 5200 m, and the semi-minor axis is ~ 340 m. The RMS misfit is 2 cm.

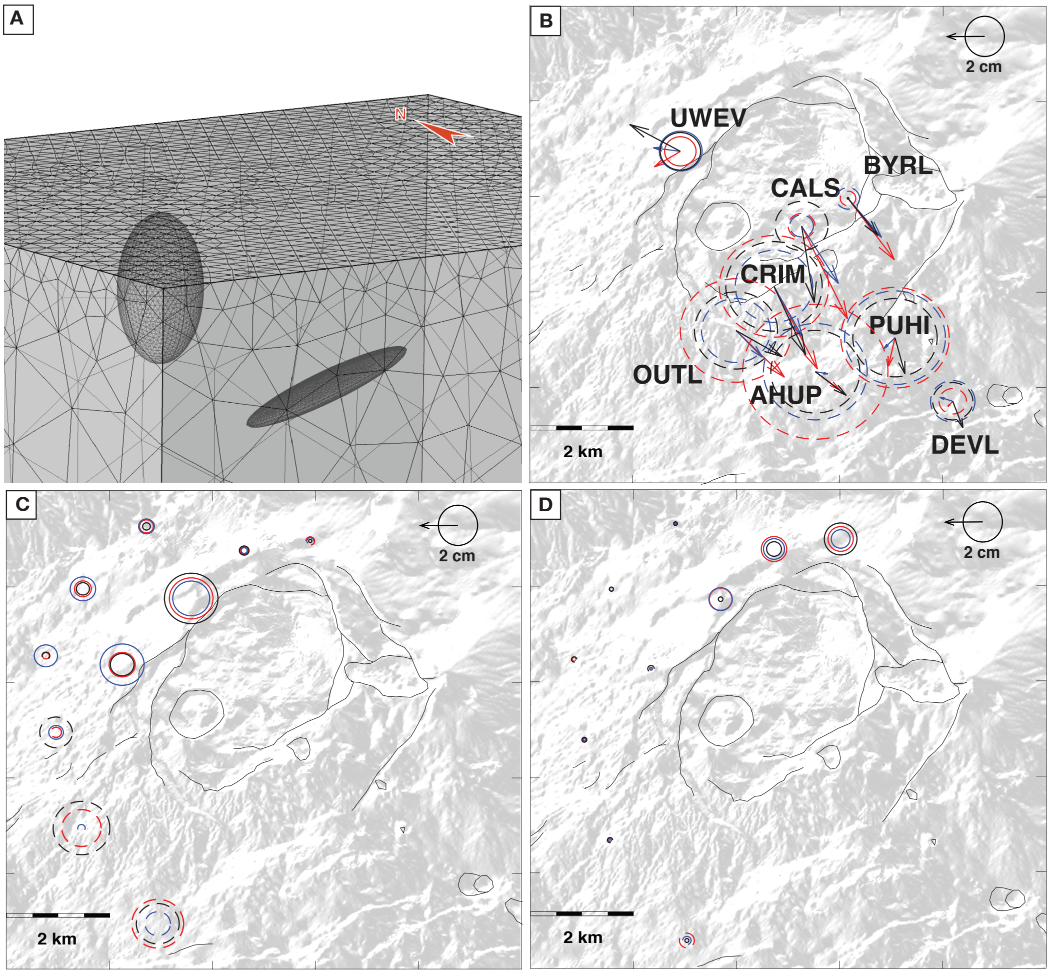

Figure 6: Nelder-Mead+ FEM inversion results compared to generalized pattern search + Yang Cervelli inversion results. All displacements are computed for the period between Nov. 4, 2018 and Mar. 16, 2019. (a): mesh of the FEM model constructed in COMSOL. (b) - (d): Comparison of displacement data (black) with Nelder Mead+FEM best prediction (blue) and Generalized Pattern Search+Yang-Cervelli best prediction (red). (b),(c),(d) are for GPS, ascending LoS, and descending LoS, respectively. All predictions are computed in the FEM model.

5 Physics based magma flux model

Conceptual models of basaltic magma reservoirs typically involve an inner, molten region (liquid), a lower "mush" region (mixture of solid and liquid), and an elastic crust (solid) that bounds the reservoir. Flow between reservoirs can be through dikes, conduits, and porous media (Wilson & Head III, 1981; Papale et al., 1998; Mastin & Ghiorso, 2000; Delaney & Gartner, 1997; Diez et al., 2005; Pollard & Delaney, 1978). We seek to model a multi-reservoir system by correctly representing the physics without overly-complicating the model. In this study, we view the magma reservoirs as magma-filled cavities embedded in elastic crust. Although a simple representation of the complex system in nature, such an approach has been proven to be useful in geodetic modeling. We use effective hydraulic conductivity to linearly relate pressure differences and magma flux and to parameterize the resistance to flow. We acknowledge that magmatic pathways can take the form of porous flow or conduits. The effective hydraulic conductivity provides a universal measure of how easily magma can flow through certain region under given pressure. For simplicity, we assume constant magma density in space and time.

To quantitatively assess the connectivity between the HMM, SC, and ERZ reservoirs, we propose a physics-based flux model in the form of a system of ordinary differential equations (ODEs). These ODEs describe the time evolution of both magma flux and reservoir pressure in a multi-reservoir system (Fig. 7). We neglect momentum balance, which dictates the short-term dynamics of pressure variations within reservoirs. The mass flux of the system is dictated by two fundamental relationships:

$$q = k\Delta p \tag{3a}$$

$$\frac{\partial p}{\partial t} = \frac{q}{V\beta} \tag{3b}$$

where k is effective hydraulic conductivity, q is volumetric flux rate, p is reservoir pressure, Δp is the pressure difference between the two connected reservoirs, V is the magma chamber volume, and β the total compressibility (combined compressibility of the magma chamber and the magma therein) of the reservoir. Eq. 3a states that magma flow rate is proportional to the pressure difference between the two magma reservoirs and the pathway's effective hydraulic conductivity (Mastin et al., 2008). Spatially uniform pressure gradient along a magma pathway connecting reservoirs is assumed. Eq. 3b (Segall et al., 2001) states that the rate of change of pressure inside a magma chamber varies as a function of total mass flux through the magma chamber, and is inversely proportional to both the volume and the total compressibility of the reservoir. This equation is derived from mass balance and assumed constant magma and chamber compressibility.

With the configuration of reservoirs and pathways illustrated in Fig. 7, we obtain the following expressions for volume flux through each pathway.

$$q_e = k_e(p_3 - \rho g h_{ERZ}) \tag{4a}$$

$$q_1 = k_1(p_1 - \rho g(h_{HMM} - h_{ERZ}) - p_3) \tag{4b}$$

$$q_2 = k_2(p_2 - p_1 - \rho g h_{12}) \tag{4c}$$

$$q_3 = k_3(p_2 - \rho g h_{23} - p_3) \tag{4d}$$

$$q_4 = k_4(p_\infty - p_2 - \rho g h_{24}) = -k_4 p_2 + k_4 p_{in} \tag{4e}$$

$$p_{in} = p_\infty - \rho g h_{24} \tag{4f}$$

where h is height of the relevant magma column and g is the gravitational acceleration. Variable definitions can be found in Table 3. The depth differences between reservoirs are accounted for by including magma-static pressures. Note that the elevation at which magma enters/exits a reservoir does not influence the magma flux between reservoirs due to the magma static term. We assume atmospheric pressure at the eruption site. Next, mass balance for each reservoir leads to:

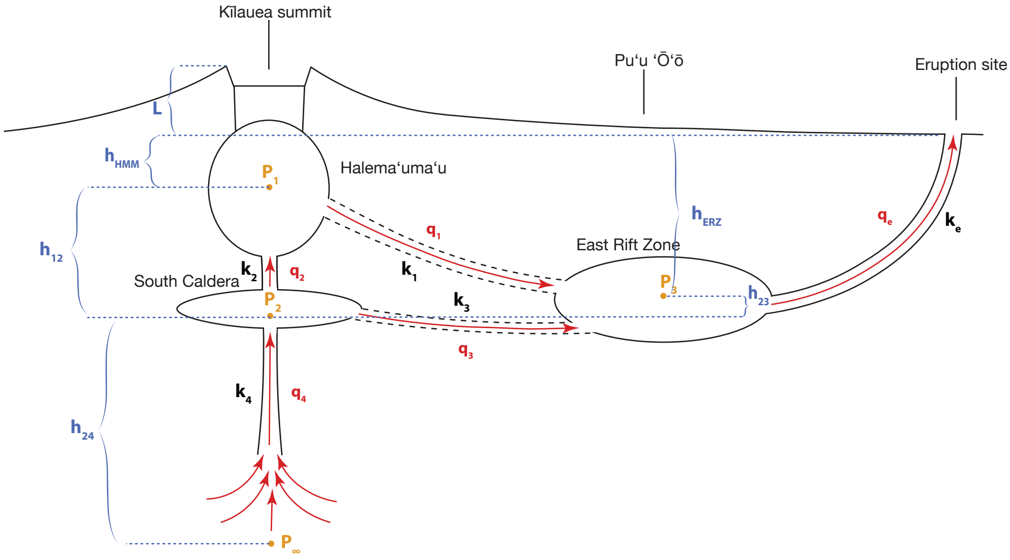

Figure 7: Schematic of the flux model. p_1, p_2, and p_3 indicate the pressure at the centroid of the HMM, the SC and the ERZ reservoir. k indicates the effective hydraulic conductivity of pathways that connect magma reservoirs and the eruptions site. h indicates elevation difference between reservoirs. q indicates volume flux. L indicates the elevation difference between the summit and the eruption site, for which we use 1000 m.

$$\frac{dp_1}{dt} = \frac{-q_e + q_2}{V_1\beta_1} \tag{5a}$$

$$\frac{dp_2}{dt} = \frac{-q_2 - q_3 + q_4}{V_2\beta_2} \tag{5b}$$

$$\frac{dp_3}{dt} = \frac{q_2 + q_1 + q_3}{V_3\beta_3} \tag{5c}$$

Consolidating the above equations yields the pressure rate within the HMM, SC, and ERZ reservoirs:

$$\dot{p_1} = \frac{-(k_1+k_2)p_1 + k_2p_2 + k_1p_3 + \rho g(k_1h_{HMM} - k_1h_{ERZ} - k_2h_{12})}{V_1\beta_1} \tag{6a}$$

$$\dot{p_2} = \frac{k_2p_1 - (k_2+k_3+k_4)p_2 + k_3p_3 + \rho g(k_2h_{12} + k_3h_{23}) + k_4p_{in}}{V_2\beta_2} \tag{6b}$$

$$\dot{p_3} = \frac{k_1p_1 + k_3p_2 - (k_e+k_1+k_3)p_3 + \rho g(k_eh_{ERZ} - k_1h_{HMM} + k_1h_{ERZ} - k_3h_{23})}{V_3\beta_3} \tag{6c}$$

Eqn. 6 represents a system of three coupled, first order, inhomogeneous, linear ODEs. Analytical solutions in principle exist. However, given the number of coefficients involved, the eigen-values and eigen-vectors are overwhelmingly complex snd the solution is not very insightful.

Given initial conditions on the pressure inside HMM, SC, and ERZ reservoirs and values for the constants, the pressure evolution $p_i(t)$ in the three reservoirs can be solved numerically. By convolving the displacement caused by unit pressure changes (Yang-Cervelli model) with pressure histories deduced from the dynamical model, we can compute the predicted time dependent deformation at the surface.

Variable	Symbol	Units	Bounds on the uniform part	MAP model	90% confidence interval
HMM - ERZ conductivity	k_1	$m^3s^{-1}Pa^{-1}$	$[10^{-9} \quad 10^{-5}]$	$10^{-7.5}$	$[10^{-7.6} \quad 10^{-7.4}]$
SC - HMM conductivity	k_2	$m^3s^{-1}Pa^{-1}$	$[10^{-12} \quad 10^{-8}]$	$10^{-7.9}$	$[10^{-8} \quad 10^{-7.8}]$
SC - ERZ conductivity	k_3	$m^3s^{-1}Pa^{-1}$	$[10^{-9} \quad 10^{-5}]$	$10^{-9.0}$	$[10^{-9.2} \quad 10^{-8.5}]$
Mantle - SC conductivity	k_4	$m^3s^{-1}Pa^{-1}$	$[10^{-9} \quad 10^{-5}]$	$10^{-7.9}$	$[10^{-8} \quad 10^{-7.6}]$
Mantle overpressure	p_{in}	MPa	[100 300]	169.8	[149.6 204.3]
SC volume	V_2	km^3	[2 13]	0.33	[0.28 0.47]
ERZ volume compressibility product	$V_3\beta_3$	m^3Pa^{-1}	$[10^{-3} \quad 7.5]$	0.58	[0.43 0.83]
HMM inital pressure	p_{1i}	MPa	[14 28]	13.6	[12.5 16.8]
SC inital pressure	p_{2i}	MPa	[60 120]	133.7	[127.6 144.7]
ERZ inital pressure	p_{3i}	MPa	[50 100]	47.5	[44.9 62.3]
HMM total compressibility	β_1	Pa^{-1}	$[10^{-9.4} \quad 10^{-8.8}]$	$10^{-9.47}$	$[10^{-9.5} \quad 10^{-9.4}]$
SC total compressiblity	β_2	Pa^{-1}	$[10^{-9.0} \quad 10^{-8.9}]$	$10^{-9.0}$	$[10^{-9.02} \quad 10^{-8.99}]$
ERZ centroid depth	h_{ERZ}	km	[2 4]	4.2	[4.0 4.4]

Table 3: Dynamic inversion parameters, bounds on uniform part of prior distributions, MAP model, and 90% confidence interval. The choice of prior bounds are discussed in Appendix E.

6 Dynamic inversion for the effective hydraulic conductivity of pathways

We estimate the pressure history, volume flux, and effective conductivity of various magmatic pathways (Fig. 7) by inverting GPS time series at the summit. The location, geometry, and orientation of the magma reservoirs are fixed to that of the MAP model from the static inversion. For each MCMC iteration, the flux model is used to predict time series deformation for a period of 480 days. Gaussian-tailed priors based on physical scaling and empirical evidence are used (Appendix E). The flux of each magmatic pathway is constrained to be non-negative, which corresponds to magma flow directions indicated in Figure 7. Surrogate optimization (Gutmann, 2001) is used to search for a model close to the global minimum of the objective function. We then use this model as the starting point for the MCMC inversion. We do not optimize for time series displacement from the ERZ due to the lack of GPS coverage in the area.

Results are presented for $\sim 1.7\times10^7$ iterations (Fig. 8). In the MAP model, k_1, k_2, and k_4 are on the order of 1×10^{-8} $m^3s^{-1}Pa^{-1}$, and k_3 is on the order of 1×10^{-9}

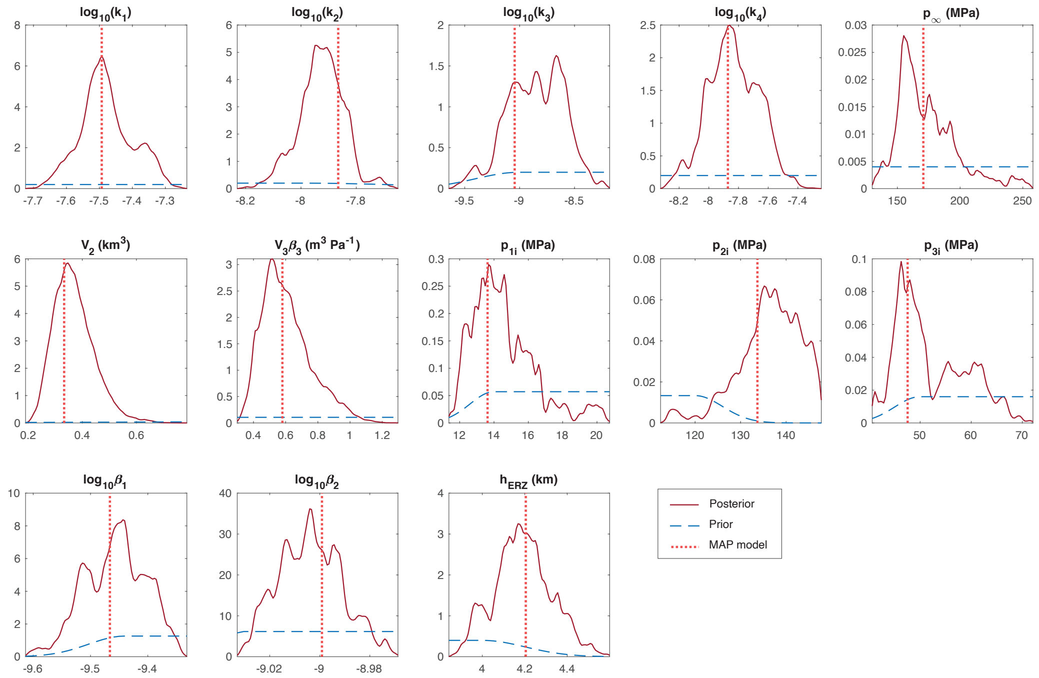

Figure 8: Posterior PDFs from the dynamic inversion after more than 1.7×10^6 MCMC iterations. Prior distributions are in blue dashed line; posterior distributions are in dark red; MAP model is in red dotted line. Gaussian tailed uniform distributions are used as priors, where the standard deviation of the tail is one tenth the width of the uniform part.

$m^3s^{-1}Pa^{-1}$. Approximately 80% of the variance in the time series data can be explained by the prediction of the MAP model (Fig. 2). Notable deviance from data exists in the east component of CALS, CRIM, and UWEV, the north component of UWEV, as well as the vertical component of CALS. We used the MAP model from the static inversion for the geometry, location, and orientation of the two summit reservoirs, which yielded relatively large residual in GPS offsets at near-caldera stations. Therefore, large misfits in temporal deformation at these stations are to be expected.

7 Discussion

7.1 Location and geometry of summit reservoirs

The estimated location, geometry, and orientation of HMM and SC (Fig. 3) reservoirs are required by features in the deformation data. Both vertical and horizontal components of the SBAS cumulative displacement maps exhibit opposite-signed displacements caused by HMM and SC reservoirs (Fig. 5). The magnitudes of the east-west displacements associated with HMM are comparable, indicating a relatively symmetrical and vertically oriented magma body. The large vertical to horizontal displacement ratio south of the caldera requires the SC reservoir to be oblate. The displacements south of the caldera exhibit larger eastward than westward displacements, which requires a northwest dipping SC source.

The static inversion yielded a tightly constrained centroid depth for the SC reservoir. The MAP model indicates a depth of ~ 3.63 km, with a 90% confidence interval between 3.5 and 3.9 km below the surface (defined by the elevation of GPS station NPIT,

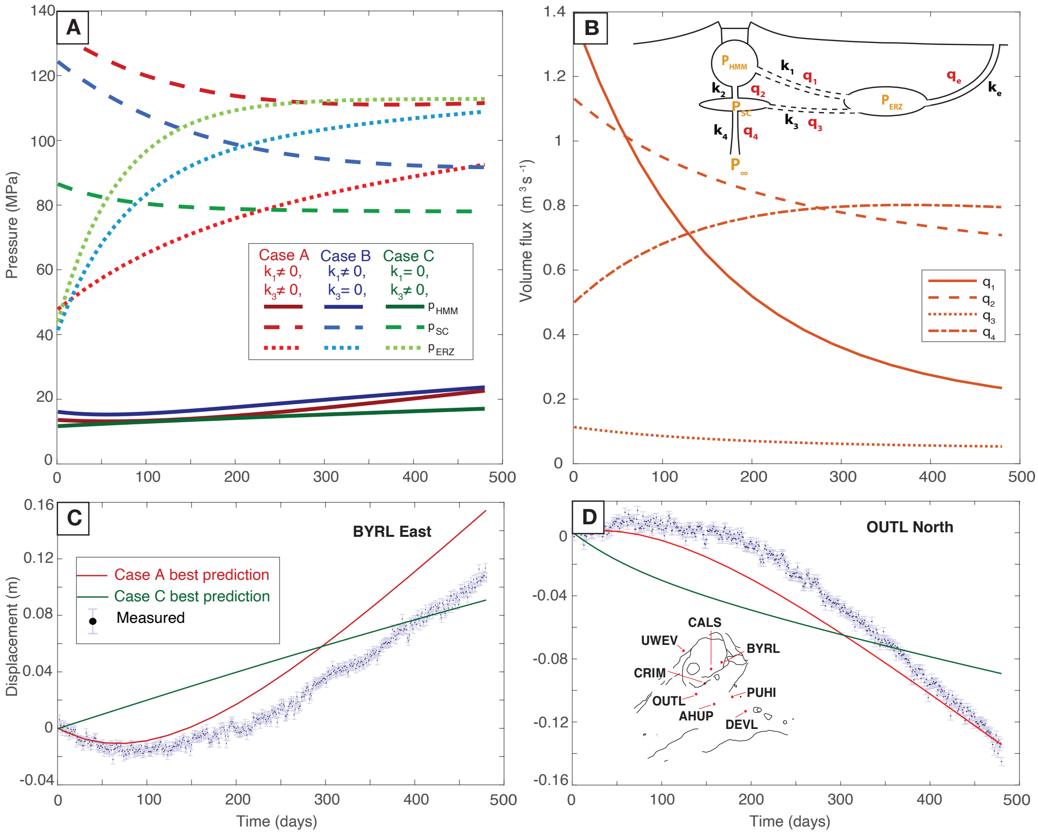

Figure 9: Pressure, volume flux and displacement over time. (a) Predicted pressure evolution inside HMM, SC, and ERZ for three different cases. Case A (shades of red): both HMM-ERZ and SC-ERZ are open. Case B (shades of blue): SC-ERZ is closed. Case C (shades of green): HMM-ERZ is closed. Solid, dashed, dotted lines indicate pressure evolution for HMM, SC, and ERZ, respectively. (b) Predicted volumetric fluxes over time. Inset shows the corresponding flux q and effective hydraulic conductivity k. (c), (d) Best-fit predictions from Case A and Case C versus GPS time series displacements for BYRL East and OUTL North, respectively.

1132 m above sea level). As far as the authors are aware of, this is the best resolved depth of the SC reservoir.

7.2 Depth of the ERZ reservoir

The dynamic inversion yielded a ERZ reservoir centroid depths of $4-4.4$ km below the surface (Fig. 8), deeper than the 2.3 km from the static inversion. This is likely due to the fact that geodetic data is more sensitive to the shallower, active part of the reservoir. In the context of the flux model, ERZ has to be deeper than SC to maintain a favorable pressure gradient that drives magma into the ERZ when its pressure approaches SC's pressure (Fig. 9). Our inferred depth for the ERZ reservoir is consistent with the notion of a "deep rift zone" (Ryan, 1988), which is inferred to be 3 - 9 km below sea level and fed by downward draining of magma from the summit reservoirs (Poland et al., 2014).

7.3 Hydraulic connection between summit reservoirs and ERZ

One of the central questions this paper seeks to address is whether the ERZ reservoir is connected to the summit system via HMM or SC, or both. The two end member scenarios are of interest because the former indicates that magma supply at Kīlauea inevitably goes through the shallow HMM reservoir before flowing towards the ERZ. The later would suggest that magma can bypass HMM before reaching the ERZ. The posterior PDFs indicate that, k_3 (SC-ERZ pathway) is likely an order of magnitude smaller than k_1 (HMM-ERZ pathway), k_2 (SC-HMM), and k_4 (mantle-SC).

To better assess the two end member cases of summit - ERZ connections, we use MATLAB optimization algorithms (Gutmann, 2001; Audet & Dennis Jr, 2002) to search for the best fit models that satisfy each case (Fig. 9). If the best prediction from one configuration can not fit the data acceptably well, we can reject the case as a probable configuration for summit-ERZ connections. We search over the same model space (Table 3) as that used in the dynamic inversion (Case A), except that in one case we close off the SC-ERZ pathway (Case B), and in the other close off the HMM-ERZ pathway (Case C). When SC-ERZ is closed off, the second derivatives (or curvature) of pressure history in all reservoirs have the same sign as those in the MAP model of Case A (Fig. 9). However, when we close HMM-ERZ pathway, the second derivative of the predicted ERZ pressure history has the opposite sign compared to that in Case A. In other words, p_{HMM} from Case A decreases slightly before increasing over time (Fig. 9), whereas p_{HMM} in Case C increases monotonically.

Because surface displacement is linear in pressure change, and Case A fits the data well, we would not expect the best prediction from Case C to fit the time series displacements. That is indeed the case: at BYRL, the east component of GPS first moved slightly west before moving east (Fig. 9 c). In the best-fit prediction, the east component monotonically moved eastward. For OUTL's north component, data shows that the southward displacement accelerated over time. Case C's best fit model, however, predicts decelerating southward displacement (Fig. 9 d).

The fact that only Case A and B fit the data can be understood as the following: when HMM-ERZ is closed, HMM has a net influx of magma due to the higher overpressure in SC, resulting in monotonically increasing pressure in HMM. Persistent net magma influx into HMM is not consistent with deformation time series. Therefore, the shallow connection between HMM and ERZ must exist. This is in agreement with Cervelli and Miklius (2003), who argued for a direct connection between HMM and the ERZ based on: 1. A shallower pathway is more likely to remain open when magma pressure inside the pathway is low; 2. without a shallow pathway between HMM and the ERZ, HMM's deflation implies magma draining back to SC.

To test whether magma could drain from HMM to SC immediately after the cessation of the collapse events, we ran an optimization without forcing magma to flow from SC to HMM, and keeping all pathways open. We found a best-fit model virtually the same as the MAP model, with magma flowing from SC to HMM. Therefore, it is not plausible that the deflation of HMM immediately after the cessation of the collapse events is associated with magma draining into the SC. Although we can not preclude that ERZ is hydraulically connected to SC from the available time series data, our analysis does suggest strongly that the deeper SC-ERZ pathway is much more resistant to magma flow, at least during the post-collapse period. If it can be shown that the hydraulic connectivity of the plumbing system in the co-collapse period is similar to that of the post-collapse period, it may imply that most of the magma erupted in 2018's Lower East Rift Zone eruption was supplied directly from the HMM reservoir.

7.4 Pressure and magma flux

The initial pressure in the HMM, SC, and ERZ reservoirs are estimated to be 13.6, 133.7, and 47.5 MPa, respectively. The ERZ initial pressure, p_{3i}, appears to be smaller than expected for an estimated ERZ reservoir depth of 4.2 km. This could result from trade-offs between the initial pressure in the ERZ and HMM, as seen in Eqn. 4b. If p_1 and p_3 increase by the same amount, the flux between HMM and ERZ, q_1, does not change. Furthermore, increasing p_1 only changes q_2 slightly because p_2 is much larger than p_1. Increasing p_3 will change the value of q_3. However, because q_3 is small compared to other fluxes (k_3 is much smaller than either k_1, k_2, or k_4), the overall dynamics of the system does not change significantly. It is verified through forward calculation that a higher p_{1i} and p_{3i} can fit the data as well as the MAP model does.

Through the dynamic inversion, we infer that pressure within the SC reservoir decreased by ~ 10 MPa during the 480 day modeling period, whereas the pressure in HMM and the ERZ increased by about 10 MPa and 40 MPa, respectively (Fig. 9). The ERZ pressure increase is comparatively high. However, a larger value of $V_3\beta_3$ would lead to a smaller pressure increase within the ERZ (Fig. F1).

The predicted magma fluxes q_1, q_2, and q_3 decrease monotonically, indicating a decrease in magma supply rate from the summit to ERZ and from SC to HMM (9 b). Such trends are consistent with pressure increases inside HMM and ERZ, which lowers the driving pressure of magma flow into these two reservoirs. The increasing flux from the mantle, q_4, results from a gradual decrease in pressure within the SC reservoir.

8 Conclusions

Through analysis of InSAR and GPS data, we report unique post-collapse simultaneous inflation and deflation at Kīlauea's summit, as well as inflation in the East Rift Zone. We constrain the location and geometry of two distinct summit reservoirs via Bayesian inversion. We check the accuracy of this inversion using a fully 3D finite element model of the two reservoirs. The centroid depth and geometry of the ERZ reservoir is estimated using similar methods. A physics-based flux model is devised to simulate the post-collapse, time-dependent deformation at Kīlauea's summit. By inverting the time series displacements with the flux model, we obtain constraints on the effective conductivity of Kīlauea's various magmatic pathways. Our main findings are:

1. Simultaneous inflation and deflation at Kīlauea's summit clearly indicates that HMM and SC are hydraulically distinct magma reservoirs, rather than different compartments of the same reservoir.

2. Inversion of GPS and InSAR displacements, assuming homogeneous half-space magma chamber models, demonstrates that the centroid of the SC reservoir is ~ 3.6 km below surface, with a 90% confidence interval between 3.5 and 3.9 km.

3. A magmatic pathway between the HMM reservoir and the ERZ is required to explain the post 2018 caldera collapse GPS time series. The effective hydraulic conductivity of the inferred SC-ERZ pathway is an order of magnitude lower and could be zero. If the hydraulic connectivity of the plumbing system did not change significantly from that during the co-collapse period, most of the magma erupted in 2018's Lower East Rift Zone eruption was supplied directly from the HMM reservoir.

Future work will focus on modeling time dependent deformation from pre- and co-collapse periods to better constrain the hydraulic connectivity of the plumbing system and understand whether these quantities change with time.

Appendix A Estimating covariance matrices for GPS noise

Estimating the amplitude of time dependent noise for GPS stations is challenging due to the persistent inflation-deflation cycles in the summit region. Assuming that random walk noise dominates time-dependent noise, we estimate the amplitude of white and random walk noise by fitting BYRL's vertical component time series with a third-order polynomial function. Optimization is done by maximizing the likelihood function (Eqn. 2) with a noise covariance that combines white and random walk noise. For the duration of the time series used in the dynamic inversion (480 days), the estimated random walk noise amplitude is consistently small ($< 1\mathrm{mm}/\sqrt{\mathrm{year}}$) compared to that of the white noise. Therefore, in the dynamic inversion we assume only white noise during the observation period. We also assume that the white noise amplitude for the same component of different summit GPS stations is the same, based on the fact that summit GPS stations have identical instrumentation and are located in a relatively small geographic region. The resulted white noise amplitude for east, north, and vertical component of GPS time series are: $\sigma_E = 0.0032$ m, $\sigma_N = 0.0027$ m, $\sigma_U = 0.0089$ m.

Appendix B InSAR time series analysis and noise covariance matrices

To explain our workflow, we highlight the most essential components of the SBAS algorithm (Berardino et al., 2002). Consider M interferograms formed from N SAR images taken in the same area. On a pixel-by-pixel basis, we have a vector of N unknown phase values and a vector of M known phase differences:

$$\vec{\phi}^T = [\phi(t_1), ..., \phi(t_N)] \tag{B1a}$$

$$\delta\vec{\phi}^T = [\delta\phi_1, ..., \delta\phi_M] \tag{B1b}$$

To obtain a physically sound solution, Berardino et al. (2002) replace the unknowns with the mean phase velocity between adjacent time acquisitions, which has the form:

$$\vec{v}^T = [v_1 = \frac{\phi_1}{t_1 - t_0}, ..., v_N = \frac{\phi_N - \phi_{N-1}}{t_N - t_{N-1}}] \tag{B2}$$

where t_0, t_1,..., t_N are the acquisition times of the N SAR images. Therefore, the relationship between phase velocity and phase differences is:

$$\boldsymbol{B}\vec{v} = \delta\vec{\phi} \tag{B3}$$

$\boldsymbol{B}$ is a $M \times N$ matrix, the entries of which are the differences between acquisition times and 0's. Due to the asymmetry of $\boldsymbol{B}$, the linear system is inverted in the minimum-norm sense using the Moore-Penrose inverse.

The differential phase $\delta\vec{\phi}$ is the sum of at least the following differential phase components:

$$\delta\vec{\phi} = \delta\vec{\phi}_{topo} + \delta\vec{\phi}_{defo} + \delta\vec{\phi}_{atm} + \delta\vec{\phi}_{orb} + \delta\vec{\phi}_{decorr} + \delta\vec{\phi}_{unwrap} \tag{B4}$$

where $\delta\vec{\phi}_{topo}$ is the residual topographic differential phase; $\delta\vec{\phi}_{defo}$ is the phase difference attributed to surface displacement between acquisition times; $\delta\vec{\phi}_{atm}$ is the differential phase due to the differences in propagation delay through the atmosphere between SAR acquisitions; $\delta\vec{\phi}_{orb}$ is the differential phase due to uncertainties in satellite orbits; $\delta\vec{\phi}_{decorr}$ represents the phase noise resulted from change in scattering properties of the resolution element over time; $\delta\vec{\phi}_{unwrap}$ is unwrapping error. Phase unwrapping errors are accounted for by masking the SBAS derived cumulative displacement maps with number of integer closures. Topographic phase is likely minor except inside the caldera, where the topographic relief is high. However, much of the signal in the caldera is masked out due to high likelihood of unwrapping errors. Assuming orbital error is small, temporal decorrelation and atmospheric delay are the major sources of noise in the differential phase.

Methods for propagating temporal decorrelation and atmospheric noise from individual interferograms to time series displacements have been developed (Agram & Simons, 2015), but incorporating the full spatial-temporal covariance matrix into SBAS remains computationally challenging. Given M interferograms formed from N SAR images, and each interferogram has P pixels, the total covariance matrix is of size $MP\times MP$. For computational tractability, we maintain a typical pixel-by-pixel approach in our SBAS procedure. This approach is based on two assumptions: 1. both the atmospheric and temporal decorrelation phase noise are normally distributed with zero mean; 2. there is no spatial correlation between phase noises. Therefore, we treat the atmospheric phase as signal and the decorrelation phase as noise in the SBAS inversion, as reflected in the weighting scheme (Eqn. B7).

We use a temporal decorrelation covariance matrix, Σ_p^t, to weight the SBAS inversion (Tough et al., 1995; Guarnieri & Tebaldini, 2008). This weighting scheme favors pixel pairs with shorter temporal baselines and thus higher temporal correlation over temporally decorrelated pixel pairs. To get Σ_p^t, we first compute the coherence $\rho_{p,m}$ for each pixel p in interferogram m using the standard coherence estimator:

$$\rho_{p,m} = \frac{\sum_{x,y}^{k,l} s_{1x,y} s_{2x,y}^{*}}{\sqrt{\sum_{x,y}^{k,l} s_{1x,y} s_{1x,y}^{*} \sum_{x,y}^{k,l} s_{2x,y} s_{2x,y}^{*}}} \tag{B5}$$

where x, y are indices of the pixels over a $k\times l$ pixel region; s_1 and s_2 denote the complex values from two SAR acquisitions. The temporal decorrelation variance can then be related to the coherence by the following expression, in the limit of Cramer-Rao (16 looks in our case):

$$\sigma_{p,m}^2 = \frac{(1-\rho_{p,m}^2)}{2L\rho_{p,m}^2} \tag{B6}$$

where $\rho_{p,m}$ is the coherence of pixel p in interferogram m and L is the number of looks for each pixel. In keeping with common practice, we only use the diagonal form of Σ_p^t, $diag[\sigma_{p,1}^2, \sigma_{p,2}^2, ..., \sigma_{p,m}^2, ..., \sigma_{p,M}^2]$, to weight the SBAS inversion. Let $\boldsymbol{P} = (\Sigma_p^t)^{-1}$ be the weight matrix, we have a vector of average LOS velocity between the time of SAR acquisitions:

$$\vec{v} = (\boldsymbol{B^T P B})^{-1} \boldsymbol{B^T P} \delta\vec{\phi} \tag{B7}$$

By integrating $\vec{v}$ over time intervals between SAR acquisitions, we obtain the cumulative displacement over time $\vec{d_p}(t)$:

$$\vec{d}_p = \boldsymbol{\tau} \cdot \vec{v}_p \tag{B8a}$$

$$\boldsymbol{\tau} = \begin{bmatrix} \Delta t_{12} & 0 & \dots & 0 \\ \Delta t_{12} & \Delta t_{23} & 0 & \vdots \\ \vdots & & \ddots & \vdots \\ \Delta t_{12} & \Delta t_{23} & \dots & \Delta t_{N-1N} \end{bmatrix} \tag{B8b}$$

Differential phase measurements are defined relative to a spatial reference point and need to be calibrated. We choose the pixel co-located with GPS station CNPK as the reference point for the entire stack of interferograms. Post SBAS analysis, we calibrated the displacement time series of this pixel, so that $\vec{d}_{CNPK}$ is consistent with LOS projected GPS time series displacement from CNPK. A comparison between LoS-projected GPS and SBAS LoS displacements at co-located pixels (Fig. B1) demonstrates the overall agreement between inverted SBAS time series displacement with GPS. To compute the average velocity for each pixel, we fit a liner model to the sub-period between Nov. 4, 2018 and Mar. 16, 2019, during which the temporal displacements approximate linear variations. We then multiply the average deformation velocity by the duration of the sub-period (133 days) to obtain cumulative displacements for each pixel (Fig. 1). This approach of computing cumulative displacement minimizes errors introduced by the scattering of displacements at each acquisition.

We estimate the spatial covariance matrix, Σ_p^s (p = 1,2,...,P) by applying a variogram to the cumulative displacement map, similar to the application of a variogram to individual interferograms (Emardson et al., 2003; Lohman & Simons, 2005). This approach assumes that the noise is spatially isotropic. Therefore, the covariance between two points separated by a scalar distance is only dependent on the distance, not on the location of these two points. The cumulative displacement map exhibits large signals due to deformation, which preclude direct sampling of this map to calculate the variance-covariance matrix. Therefore, we filter the cumulative displacement map with a high-pass Gaussian filter, the kernel of which is a 310 by 310 pixel square matrix with a standard deviation of 50 pixels (each pixel is 30 m $\times$ 30 m). This procedure effectively removes deformation signals of comparable size to the filter kernel. A side effect of the high pass filtering is that atmospheric effect on the same length scale as the deformation ($\sim$ 10 km) is removed from the cumulative displacement map.

We then compute the structure function (Emardson et al., 2003; Lohman & Simons, 2005) by randomly selecting 1×10^6 pixel pairs from the filtered cumulative displacement map, excluding pixels within 4 km of the approximate center of deformation (to avoid residual deformation signals). The empirical structure function is defined as:

$$S(r) = \frac{1}{N}[\delta\phi(\vec{\boldsymbol{x}}) - \delta\phi(\vec{\boldsymbol{x}} + \vec{\boldsymbol{r}})]^2 \tag{B9}$$

where r is the binned distance between pixel pairs and N is the number of pixel pairs in each bin. The empirical structure function can be fit with $S(r) = s[1 - exp(-r/\Delta)]$, where r is the variable distance between pixel pairs, s is the variance, and Δ is the characteristic distance that controls the change in variance with r. With this relation, we can compute the covariance for each pixel with regard to a reference pixel using the parametric function, $C(r) = s[\exp(-r/\Delta)]$.

We down-sampled the cumulative displacement map using a quadtree algorithm based on a threshold variance. Following Lohman and Simons (2005), we compute the spatial covariance Σ between quadtree leaves with indices i and j using the above parametric form of the spatial covariance matrix (following the notation of Anderson et al.,

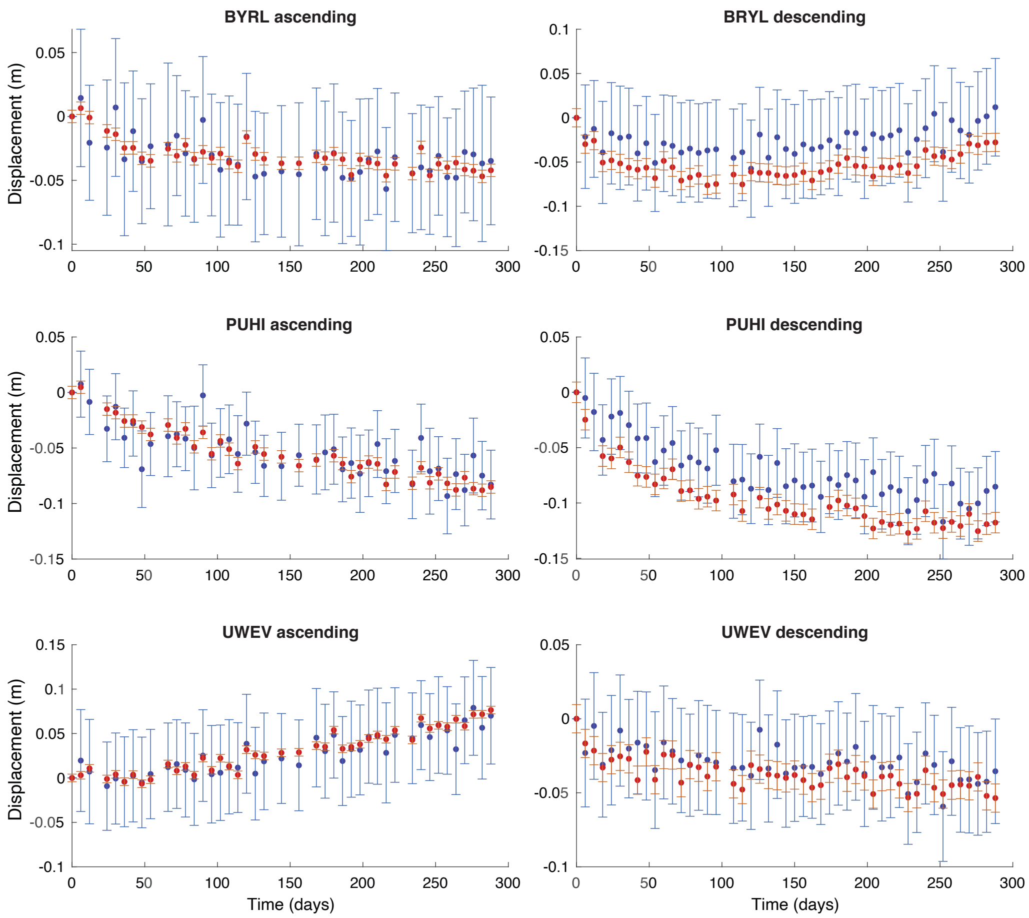

Figure B1: Comparison of SBAS LoS time series displacement (blue points) with LoS-projected GPS time series displacement (red points). Error bars show one standard deviation. GPS error is assumed to be purely white noise (Appendix A), and error of SBAS time series only accounts for temporal decorrelation noise (Appendix B).

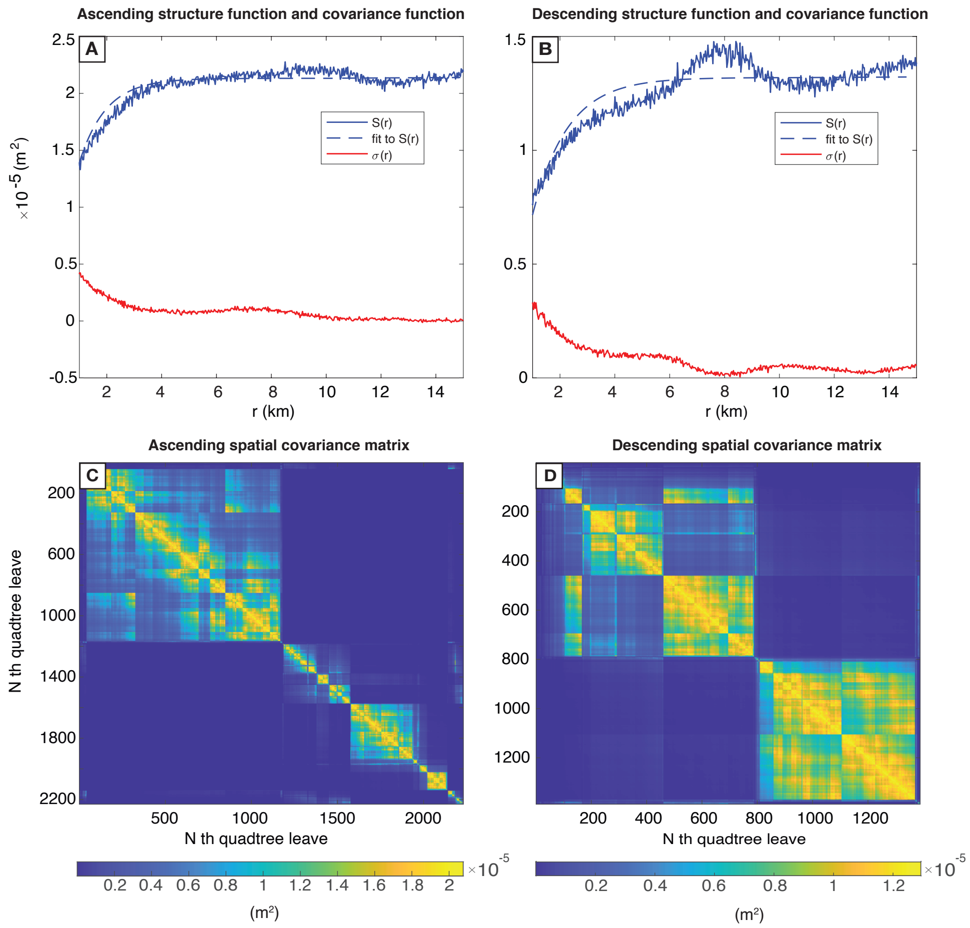

Figure B2: (a), (b): Empirical structure function $S(r)$ and covariance function $\sigma(r)$ for ascending and descending cumulative displacement maps, respectively. (c), (d): spatial covariance matrices of atmospheric noise for ascending and descending cumulative displacement maps, respectively.

2019):

$$\Sigma_{i,j} = \frac{1}{n_i, n_j} \sum_{k=1}^{n_i} \sum_{l=1}^{n_j} C_{k,l}(\nabla_{i,j,k.l}) \tag{B10}$$

where n_i and n_j are the number of points in quadtree leaves i and j; $\nabla_{i,j,k.l}$ is the Euclidean distance between the k th and l th pixels in the quadtree leaves i and j, respectively. The resulting spatial covariance matrices for ascending and descending cumulative displacement maps (Fig. B2) show blocks of high covariance values among clusters of quadtree leaves. This is expected, because the quadtree algorithm produces smaller, closely-spaced leaves in areas with high-spatial frequency noise. The high covariance among these clustered quadtree leaves are captured through the spatial covariance matrix.

Appendix C Optimum weighting of GPS vs. InSAR in static inversion

The weight is defined as the numerical value multiplied to the covariance-weighted L2 norm of GPS residuals. For each weight, we use surrogate optimization (Gutmann, 2001) to search for a model that minimizes misfit to the combined GPS and InSAR data

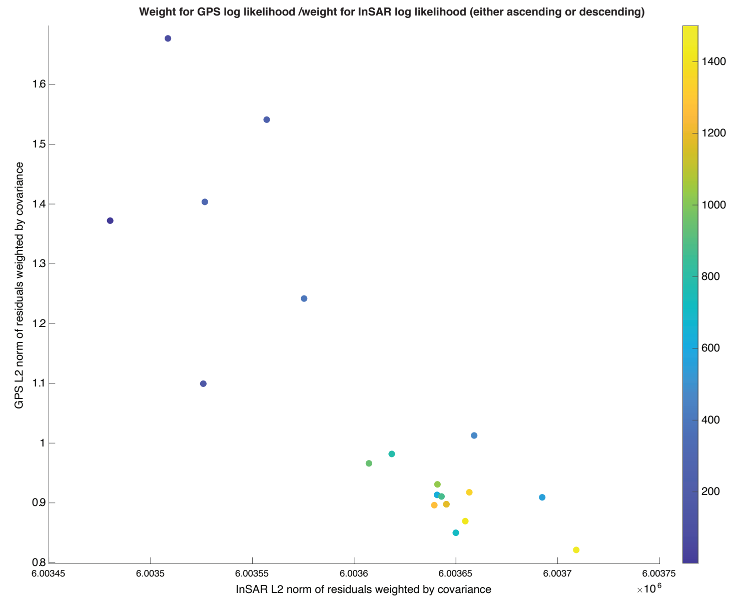

Figure C1: Weighted residuals as a function of weighting for GPS vs. InSAR data. Color bar shows the value of weight for GPS.

sets. As shown in Fig. C1, the larger the weight for GPS residuals, the lower the misfit to GPS, as expected. We take a weight of 1000 for the static inversion because it significantly reduces misfit to GPS without overly compromising fit to InSAR data.

Appendix D Static inversion using full vs. reduced data set

Because the reduced data set (3 component displacement from 8 GPS stations and 10 LoS displacement data points) is used for the Nelder Mead + FEM inversion, we need to understand the distinction between using the reduced data set and the full data set. We run a generalized pattern search optimization (Audet & Dennis Jr, 2002) + Yang-Cervelli inversion on the reduced data set and the full data set for 50 iterations to check whether the two inversions yield similar parameter estimates, using the same inversion algorithm and forward model. Indeed, the best-fit model from the full data set inversion is very similar to that from the reduced data set inversion (Table. D1)

The mean of the normalized difference between the full-data and the reduced-data best fit parameters is 7%, which indicates that the two models are fairly similar. Notable differences are in the pressure changes of HMM and SC, but the geometry, horizontal location, and the depth of HMM and SC are consistent. Therefore, inversion results are not sensitive to full versus reduced data set.

Appendix E Prior constraints on temporal inversion parameters

There are 13 parameters of interest in the lumped-parameter flux model (Table. 3). We invert for $V_3\beta_3$, instead of V_3 and β_3 independently, because we lack the constraint on the ERZ reservoir's volume. In this section, we deduce prior constraints on these parameters with judicious assumptions. To account for the uncertainties in the analyses, we use the bounds deduced in this section as the limits on the uniform part of the Gaussian-tailed prior distribution (Table 3). The "tail" of either end of the distribution is assigned a standard deviation equivalent to 10% the width of the uniform part.

parameter	units	full data inversion	reduced data inversion
a_{HMM}	km	0.557	0.557
b_{HMM}	km	0.469	0.469
d_{HMM}	km	-2.22	-2.092
α_{HMM}	unit-less	1.9	1.9
Δp_{HMM}	MPa	1.48	1.578
a_{SC}	km	1.757	1.757
b_{SC}	km	-2.931	-2.931
d_{SC}	km	-3.942	-3.446
α_{SC}	unit-less	0.158	0.158
Δp_{SC}	MPa	-1.215	-1.390
ϕ_{SC}	unit-less	121	121
ψ_{SC}	unit-less	-33	-48

Table D1: Best fit models from generalized pattern search + Yang Cervelli inversion using reduced and full data sets.

E1 Effective hydraulic conductivity

Dikes, cylindrical conduits, and porous flow can all produce pressure dependent flow (Section 5). However, by assuming flow through cylindrical conduits, we can derive a range of physically plausible effective hydraulic conductivity, k, through the scaling relationships of Hagen-Poiseuille flow, assuming linear pressure gradient:

$$k = \frac{\pi R^4}{8\eta L} \tag{E1}$$

where R is the radius of the conduit, η is magma dynamic viscosity, and L is the length of the conduit. Assuming constant hydraulic conductivity in time, we can, to the first order, estimate the range of possible radii for the pathways through scaling laws: magma solidification and melt-backs are the two end member behaviors of the balance between along-dike advective heat transport and magma flow velocity. The dimensionless ratio between advective heat transport and conductive heat transfer provides a measure of the relative importance of each mode of heat transport (Bruce & Huppert, 1989). For a ratio $\gg 1$, advective heat transfer dominates, and the conduit will widen due to melt-back. For a ratio $\ll 1$, conductive dissipation of heat results in the freezing of magma, leading to a narrowing pathway (Gonnermann & Taisne, 2015). As such, the conduit radius must allow the ratio to be of order 1 so that its diameter can be maintained. This ratio is expressed as following. Consider magma flow along a conduit in the z direction, we have the advection-diffusion equation, the linearization of the advection term, and the linearization of the conductive term, respectively:

$$\frac{\partial u}{\partial t} + w\frac{\partial u}{\partial z} = \kappa\frac{\partial^2 u}{\partial x^2} \tag{E2a}$$

$$w\frac{\partial u}{\partial z} \sim w\frac{\Delta u_L}{L} \tag{E2b}$$

$$\kappa\frac{\partial^2 u}{\partial x^2} \sim \kappa\frac{\Delta u_D}{D^2} \tag{E2c}$$

where u is the temperature of the magma; w is the flow velocity in the z direction; x is the radial direction from the central axis of the conduit; κ is the thermal diffusivity of the host rock (basalt); D is the diameter of the conduit. Because the magma is not solidifying anywhere in the conduit (per the dimensionless ratio argument), the characteristic temperature change over the length, Δu_L, and over the radius, Δu_D, must be of similar magnitude. Therefore,

$$\Pi \sim w\frac{\Delta u}{L}/\kappa\frac{\Delta u}{D^2} = \frac{wD^2}{\kappa L} \tag{E3}$$

For Hagen-Poiseuille flow, the mean linear velocity across the diameter of the pathway is:

$$\bar{w} \sim \frac{\Delta p(0.5D)^2}{8L\eta} \tag{E4}$$

where p is the pressure change along the flow direction at the two ends of the pathway. Plugging the mean linear velocity into Eqn. E3, we have:

$$\Pi \sim \frac{D^4\Delta p}{32\kappa\eta L^2} \tag{E5}$$

Assuming the dynamic viscosity of basalt is 150 $\mathrm{Pa \cdot s}$, the magmatic over-pressure, Δp, for p_1, p_2, and p_∞ are less than 10 MPa (the upper bound is laboratory measured tensile strength of basalt (Tait et al., 1989)), and the thermal diffusivity of basaltic lava is 5×10^{-6} $\mathrm{m^2s^{-1}}$ (Hartlieb et al., 2016). For k_2, L is 3 km at its maximum (given the inverted locations in the static inversion). Therefore, from Eqn. E3, we have $D \sim 0.7 \sim O(-1)$. For k_1, k_3, L is $\sim$ 20 km. Therefore, $D \sim 1.7 \sim O(0)$. For k_4, L is $\sim$ 60 km, and the corresponding $D \sim 3 \sim O(0)$. Given that our estimated pathway diameters are of order -1 or 0, and the order of magnitude should be interpreted as the approximate length scale of the radii, the range of radii we consider for these pathways are 0.1 - 1 meters for k_2 and 1 - 10 meters for k_1, k_3, k_4. These two ranges of radii correspond to the effective conductivity of $O(-12) < k_2 < O(-8)$, $O(-9) < k_1, k_3, k_4 < O(-5)$.

E2 Compressibility of summit reservoirs

The total compressibility of each magma reservoir is $\beta = \beta_m + \beta_{ch}$, where β_m is the bulk magma compressibility and β_{ch} is the magma chamber compressibility. The compressibility of bulk magma is a function of pressure and temperature, which dictates the solubility of volatile species in the magma. The compressibility of the magma chamber is a function of the bulk modulus of host rock, the geometry of the chamber, and the depth to the top of the chamber. Qualitatively, magma reservoirs with large aspect ratios are more compressible than those with lower aspect ratios (Amoruso & Crescentini, 2009).

E21 Magma chamber compressibility

The compressibility of the magma chamber is defined as: $\beta_{ch} = \frac{1}{V}\frac{\partial V}{\partial p}$, where V is the volume of the magma chamber, and p is pressure. Analytical approximations for the pressure derivative in the above equation exist (Amoruso & Crescentini, 2009; Cervelli, 2013). However, Anderson and Segall (2011) demonstrated that, analytical approximation of the compressibility of a spheroid magma chamber deviates significantly from the numerical solution for a depth to effective radius ratio larger than 0.75, where the effective radius is that of a volume-equivalent sphere. For robustness, we adopt the numerical emulator approach developed by Anderson et al. (2019). The numerical emulator takes input aspect ratio and depth to the top of a spheroid and compute the corresponding chamber compressibility, assuming a crustal shear modulus of 3×10^9 Pa (Anderson et al., 2019). To compute the chamber compressibility of HMM, we take an aspect ratio of 1.1, a depth to centroid of 1.9 km, and a volume of 3.5 $\mathrm{km^3}$ (Anderson et al., 2019), which yield a chamber compressibility of 2.63×10^{-10} $\mathrm{Pa^{-1}}$. For aspect ratios between 1 and 2, variation in chamber compressibility is fairly small. Assuming a volume of 2.5×10^9 $\mathrm{km^3}$ for SC source (Pietruszka & Garcia, 1999), an aspect ratio of 0.1748, and a depth of $\sim$ 3.5 km, we obtain a magma chamber compressibility of 8.3×10^{-10} $\mathrm{Pa^{-1}}$ for SC. Given fixed aspect ratio for SC, for a volume between 2.5 and 13 $\mathrm{km^3}$, SC's chamber compressibility does not change significantly.

E22 Magma compressibility

Magma compressibility is defined as $\beta_m = \frac{1}{\rho_m}\frac{\partial \rho_m}{\partial p}$, where ρ_m is bulk magma density, and is a function of pressure-dependent mass concentrations of dissolved volatiles, exsolved volatiles, and phenocrysts (Anderson & Segall, 2011). We use the "degassing path" feature of VolatileCalc (Newman & Lowenstern, 2002) to compute the pressure-dependent mass concentration of dissolved H_2O and CO_2. For the upper bound of bulk magma compressibility, we assume closed-system degassing, and find the compressibility of bulk magma at SC's depth. Gerlach and Graeber (1985) estimated the mass concentration of water dissolved in chamber-equilibriated magma as 0.27 wt %, which is insensitive to depth below the top 50 m of the magma storage system. Due to magma oversaturation with CO_2 except near surface, the mass concentration of dissolved CO_2 can be computed from its solubility as a function of depth (Gerlach & Graeber, 1985). For a SC depth of $\sim$ 5 km, the magma contains 0.058 wt % of dissolved CO_2. Assuming closed system degassing, we calculate the mass concentration of exsolved volatiles in the magma chamber as the difference in that of parental magma and that of chamber-depth equilibriated magma (Gerlach & Graeber, 1985), which yields (0.3 - 0.27 wt % =) 0.03 wt % for H_2O and (0.65 - 0.058 wt % =) 0.59 wt % for CO_2. The mass fraction of exsolved volatiles with regard to bulk magma can be approximated as the sum of the calculated mass concentrations for H_2O and CO_2 because the volatiles are a very small weight percentage of the bulk magma. We input mass concentration of dissolved H_2O and CO_2 in magma equilibriated at SC's depth, magma temperature, and mass fraction of exsolved volatiles inside SC chamber into VolatileCalc to compute the dissolved volatile mass concentrations as a function of pressure (Newman & Lowenstern, 2002). We then compute bulk magma compressibility as a function of pressure through the derivative of bulk magma density with respect to pressure. SC approximate depth at $\sim$ 3.5 km corresponds to a magma-static pressure of 93 MPa. The true magmatic pressure inside SC must be at least a few MPa above the magma-static in order to drive magma flow into the shallower HMM and ERZ. For simplicity, we take 100 MPa for pressure in SC, which yields a bulk magma compressibility of 4.24×10^{-10} Pa^{-1}. HMM's centroid is approximately 1.9 km below the surface, corresponding to a magma-static pressure of $\sim$ 50 MPa. At this pressure, the degassing curve yields a compressibility of 1.46×10^{-9} Pa^{-1}.

E23 Total compressibility

The upper bound on SC's total compressibility is 12.54×10^{-10} Pa^{-1}. The lower bound on SC's magma compressibility is given by experimentally determined basaltic melt compressibilty, 1×10^{-10} Pa^{-1} (Murase & McBirney, 1973). Adding this value to the lower bound on SC's chamber compressibilty, we obtain 9.3×10^{-10} Pa^{-1} as the lower bound on SC's total compressibility. The largest uncertainty in SC's chamber compressibility is due to its volume. A larger SC volume makes the radius to centroid depth ratio larger, thereby increasing the chamber compressibility. The total compressibility of HMM is between 3.63×10^{-10} and 15.6×10^{-10} Pa^{-1}. Estimates for HMM correspond well with the $2 - 15 \times 10^{-10}$ Pa^{-1} range estimated by Segall et al. (2020).

E3 Depth, volume, compressibility of the ERZ reservoir

Inversion of LoS displacements from the ERZ using a Yang-Cervelli spheroid produced a centroid depth of $\sim$ 2.3 km, with a semi-minor axis (sub-vertically oriented) length of $\sim$ 340 m. Given that the true geometry of the reservoir is likely not a spheroid, and geodetic observations are most sensitive to the top, active parts of reservoirs, we use a depth range of 2-4 km below sea level for the ERZ reservoir. Because of the volume-pressure change trade-off, inversion of surface deformation does not uniquely determine the volume of the ERZ reservoir. One of the few volume estimates of reservoirs in the East Rift Zone is that of Pu'u 'Ō'ō, at $\sim 1 \times 10^7$ m^3 (Poland et al., 2014). Using this volume as the lower bound, we search for a volume between 1×10^7 m^3 and 5×10^9 m^3.

ERZ's total compressibility depends on reservoir geometry and magma volatile content. Assuming that much of the ERZ magma had undergone some degassing in the summit area, the exsolved volatile content of magma in ERZ should not be higher than that of HMM. Therefore, we infer an upper bound on magma compressibility of 1.46×10^{-9} Pa^{-1}. The lower bound is that of bubble free magma, 1×10^{-10} Pa^{-1} (Murase & McBirney, 1973). For a wide range of depths and chamber aspect ratios, the chamber compressibility is of order 10^{-10} Pa^{-1}, in which case the contribution of chamber compressibility to the total compressibility is minor. Therefore, we infer a total compressibility between 1×10^{-10} and 1.5×10^{-9} Pa^{-1}. The product of ERZ volume and total compressibility is between 1×10^{-3} and 7.5 $\mathrm{m}^3\mathrm{Pa}^{-1}$. One caveat is that, the ERZ reservoirs as a whole may behave as a dike-like feature. In that case the chamber will contribute significantly to the total compressibility, which requires higher upper bound on the volume-compressibility product. In our preliminary search over the model space, the best-fit model did not approach the upper bound, so we leave the inferred priors unchanged.

E4 Initial pressure

Prior to the caldera collapse, HMM's centroid pressure is approximately magmastatic: $p^{ms}_{HMM} = \rho_m g h_{HMM} = 2600\,\mathrm{kg\,m^{-3}} \times 9.8\,\mathrm{N\,kg^{-1}} \times 1900\,\mathrm{m} \approx 48\,\mathrm{MPa}$, which likely is an underestimate by 1 to 10 MPa due to increasing magma density at depths. Anderson et al. (2019) estimated a pressure drop of $\sim$ 25 MPa from the beginning to the end of May inside HMM. Starting on May 29, broad collapse events took place, each associated with a co-collapse pressure surge and a post collapse gradual pressure drop. Segall et al. (2020) inferred that co-collapse pressure surge is between 1 and 3 MPa. On average, post-collapse pressure drop is slightly larger than co-collapse pressure surge to produce a net deflation over three months. The cumulative pressure change due to collapse events is likely a fraction of that prior to collapse events, as reflected in the gradual decline of radial tilt measurements since the beginning of broad caldera collapse events. Assuming that the cumulative pressure drop due to the collapse events amounted to 5 to 10 MPa, a first order estimate of the initial pressure inside HMM (right at the end of collapse in August, 2018) is $\sim 14-28$ MPa. We estimate SC's initial pressure to be approximately magma-static: $p^{ms}_{SC} = \rho_m g h_{SC} = 2600\,\mathrm{kg\,m^{-3}} \times 9.8\,\mathrm{N\,kg^{-1}} \times 3500\,\mathrm{m} \approx 90\,\mathrm{MPa}$. For the dynamic inversion, we use a wide range of 60 to 120 MPa to account for the ambiguity of this estimation. InSAR data indicates that, in early May, MERZ was deflating along strike while LERZ was inflating (Neal et al., 2019), indicating magma transfer from the MERZ to the eruption site in the LERZ. However, given the lack of independent constraint on ERZ's pressure in late August, we assume that ERZ's initial pressure is close to magmastatic. With a depth to centroid between 2 and 4 km below sea level, the initial ERZ pressure is $p^{ms}_{ERZ} = \rho_m g h_{ERZ} \approx 50 - 100$ MPa.

E5 Mantle overpressure

In Hawaii, seismicity associated with melt extraction suggests that the maximum depth of melt extraction is 60 km (Nicolas, 1986). Assuming an overpressure of $\sim$ 5 MPa/km is generated due to the density contrast between melt and surrounding crustal rock, p_∞ is on the order of a few hundred MPa. Due to the generality of this estimate, we set the bounds on the prior as between 100 and 300 MPa.

Appendix F Sensitivity analysis

To assess the effect of each parameter on the pressure history of magma reservoirs, we perform a sensitivity analysis for each parameter (Fig. F1). Because surface deformation is linearly proportional to pressure change, and plotting all components of time series displacements at different stations is cumbersome, we use pressure history as a proxy for the measured time series displacements. For each parameter, we choose equally-spaced

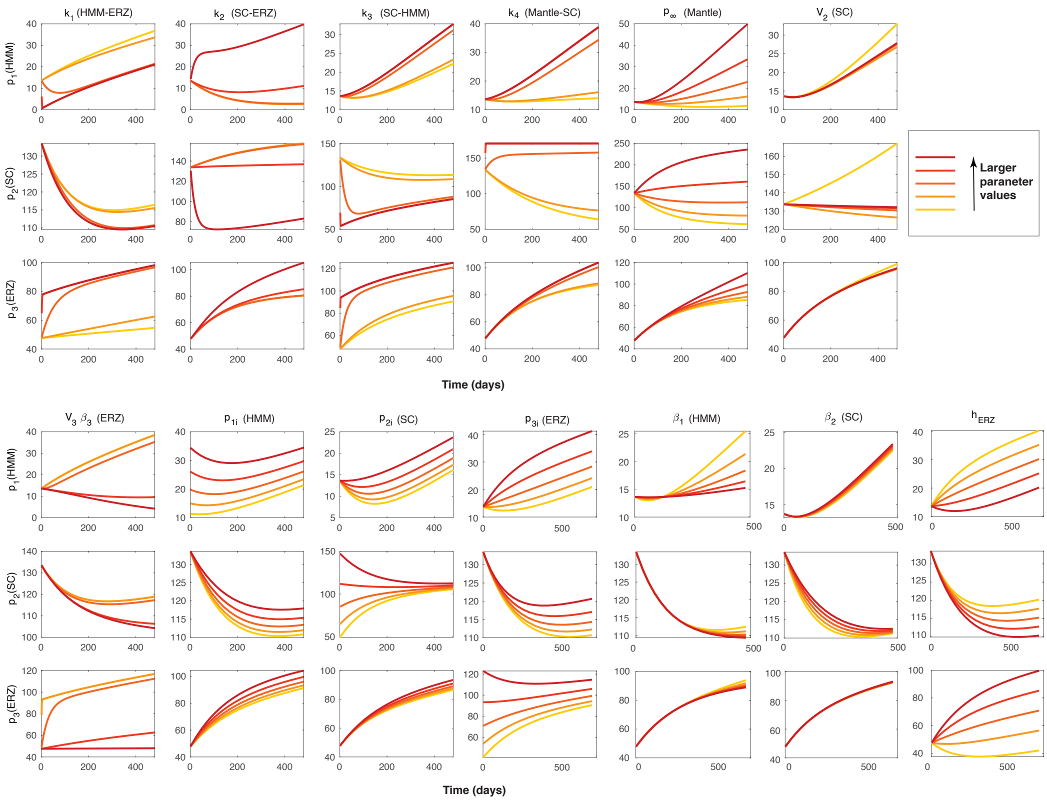

Figure F1: Sensitivity analysis for all 13 parameters. For each parameter, we choose 5 uniformly distributed values within the bounds and compute the predicted pressure history for the reservoirs, keeping other parameters' values the same as the MAP model.

5 values of the parameter in between the given bounds (Table 3) and keep the values of the rest of the parameters at MAP values. For each variation of the parameter, we compute the corresponding pressure history $p_1(t)$, $p_2(t)$, $p_3(t)$.

k_1, k_2, and k_3 have prominent influence on the curvature of pressure history. For example, increasing k_1 can cause p_1 to decrease rapidly before gradually increasing again. This behaviour is expected, because higher hydraulic conductivity between HMM and ERZ would allow magma to evacuate from HMM much faster. Increasing k_4 results in larger increase in p_1 and p_2 over time and subdued decrease in p_2. Changing p_∞, V_2, p_{2i}, p_{3i}, h_{ERZ}, $V_3\beta_3$ can result in sign change of the pressure history. For example, if the initial pressure inside SC, p_{2i}, is below certain threshold, SC will have a net influx of magma, resulting in a net increase in pressure. This scenario would correspond to an inflating SC source, which is not consistent with observations. On the other hand, in an unrealistic scenario, if the mantle pressure is below certain threshold, magma will flow from SC into the mantle source. Scenarios like this where magma flow reverses direction are not permitted in the dynamic inversion.

Acknowledgments

We thank the USGS for access to GPS data. Thanks to Dr. Kyle Anderson for helpful discussions related to the post-collapse deformation in the summit region. We also thank Prof. Howard Zebker for insights on SBAS time series analysis. GPS data are available from the UNAVCO archive (https://www.unavco.org/data/data.html). InSAR data are available from Alaska Satellite Facility's data repository (https://asf.alaska.edu/data-sets/derived-data-sets/insar/).

References

Agram, P., & Simons, M. (2015). A noise model for insar time series. *Journal of Geophysical Research: Solid Earth*, *120*(4), 2752–2771.

Amoruso, A., & Crescentini, L. (2009). Shape and volume change of pressurized ellipsoidal cavities from deformation and seismic data. *Journal of Geophysical Research: Solid Earth*, *114*(B2).

Anderson, K., Johanson, I., Patrick, M. R., Gu, M., Segall, P., Poland, M., ... Miklius, A. (2019). Magma reservoir failure and the onset of caldera collapse at kīlauea volcano in 2018. *Science*, *366*(6470).

Anderson, K., & Poland, M. (2016). Bayesian estimation of magma supply, storage, and eruption rates using a multiphysical volcano model: Kīlauea volcano, 2000–2012. *Earth and Planetary Science Letters*, *447*, 161–171.

Anderson, K., & Segall, P. (2011). Physics-based models of ground deformation and extrusion rate at effusively erupting volcanoes. *Journal of Geophysical Research: Solid Earth*, *116*(B7).

Audet, C., & Dennis Jr, J. E. (2002). Analysis of generalized pattern searches. *SIAM Journal on optimization*, *13*(3), 889–903.

Baker, S., & Amelung, F. (2012). Top-down inflation and deflation at the summit of kīlauea volcano, hawai ‘i observed with insar. *Journal of Geophysical Research: Solid Earth*, *117*(B12).

Bato, M. G., Pinel, V., Yan, Y., Jouanne, F., & Vandemeulebrouck, J. (2018). Possible deep connection between volcanic systems evidenced by sequential assimilation of geodetic data. *Scientific reports*, *8*(1), 1–13.

Berardino, P., Fornaro, G., Lanari, R., & Sansosti, E. (2002). A new algorithm for surface deformation monitoring based on small baseline differential sar interferograms. *IEEE Transactions on geoscience and remote sensing*, *40*(11), 2375–2383.

Bruce, P. M., & Huppert, H. E. (1989). Thermal control of basaltic fissure eruptions. *Nature*, *342*(6250), 665–667.

Cervelli, P. (2013). Analytical expressions for deformation from an arbitrarily oriented spheroid in a half-space.
Cervelli, P., & Miklius, A. (2003). The shallow magmatic system of kilauea volcano. *US Geol. Surv. Prof. Pap*, *1676*, 149–163.
Delaney, P. T., & Gartner, A. E. (1997). Physical processes of shallow mafic dike emplacement near the san rafael swell, utah. *Geological Society of America Bulletin*, *109*(9), 1177–1192.
Dieterich, J. H., & Decker, R. W. (1975). Finite element modeling of surface deformation associated with volcanism. *Journal of Geophysical Research*, *80*(29), 4094–4102.
Diez, M., Connor, C., Connor, L., & Savov, I. (2005). Magma dynamics and conduit growth mechanisms inferred from exposed volcano conduits at the san rafael subvolcanic field, utah. *AGUFM*, *2005*, V33A–0662.
Emardson, T., Simons, M., & Webb, F. (2003). Neutral atmospheric delay in interferometric synthetic aperture radar applications: Statistical description and mitigation. *Journal of Geophysical Research: Solid Earth*, *108*(B5).
Fialko, Y., Simons, M., & Agnew, D. (2001). The complete (3-d) surface displacement field in the epicentral area of the 1999 mw7. 1 hector mine earthquake, california, from space geodetic observations. *Geophysical research letters*, *28*(16), 3063–3066.
Fiske, S., & Kinoshita, T. (1969). Inflation of kilauea volcano prior to its 1967-1968 eruption. *Science*, *165*(3891), 341–349.
Gerlach, T. M., & Graeber, E. J. (1985). Volatile budget of kilauea volcano. *Nature*, *313*(6000), 273–277.
Gonnermann, H., & Taisne, B. (2015). Magma transport in dikes. In *The encyclopedia of volcanoes* (pp. 215–224). Elsevier.
Guarnieri, A. M., & Tebaldini, S. (2008). On the exploitation of target statistics for sar interferometry applications. *IEEE Transactions on Geoscience and Remote Sensing*, *46*(11), 3436–3443.
Gutmann, H.-M. (2001). A radial basis function method for global optimization. *Journal of global optimization*, *19*(3), 201–227.
Hartlieb, P., Toifl, M., Kuchar, F., Meisels, R., & Antretter, T. (2016). Thermo-physical properties of selected hard rocks and their relation to microwave-assisted comminution. *Minerals Engineering*, *91*, 34–41.
Keating, G. N., Valentine, G. A., Krier, D. J., & Perry, F. V. (2008). Shallow plumbing systems for small-volume basaltic volcanoes. *Bulletin of Volcanology*, *70*(5), 563–582.
Lohman, R. B., & Simons, M. (2005). Some thoughts on the use of insar data to constrain models of surface deformation: Noise structure and data downsampling. *Geochemistry, Geophysics, Geosystems*, *6*(1).
Mastin, L. G., & Ghiorso, M. S. (2000). *A numerical program for steady-state flow of magma-gas mixtures through vertical eruptive conduits* (Tech. Rep.). Department of the Interior Washington DC.
Mastin, L. G., Roeloffs, E., Beeler, N. M., & Quick, J. E. (2008). *Constraints on the size, overpressure, and volatile content of the mount st. helens magma system from geodetic and dome-growth measurements during the 2004-2006+ eruption* (Tech. Rep.). US Geological Survey.
Montagna, C. P., & Gonnermann, H. M. (2013). Magma flow between summit and pu ‘u ‘ō ‘ō at klauea volcano, hawai ‘i. *Geochemistry, Geophysics, Geosystems*, *14*(7), 2232–2246.
Murase, T., & McBirney, A. R. (1973). Properties of some common igneous rocks and their melts at high temperatures. *Geological Society of America Bulletin*, *84*(11), 3563–3592.
Neal, C. A., Brantley, S., Antolik, L., Babb, J., Burgess, M., Calles, K., . . . others (2019). The 2018 rift eruption and summit collapse of kīlauea volcano.

Science, *363*(6425), 367–374.

Newman, S., & Lowenstern, J. B. (2002). Volatilecalc: a silicate melt–h2o–co2 solution model written in visual basic for excel. *Computers & Geosciences*, *28*(5), 597–604.

Nicolas, A. (1986). A melt extraction model based on structural studies in mantle peridotites. *Journal of Petrology*, *27*(4), 999–1022.

Owen, S., Segall, P., Lisowski, M., Miklius, A., Murray, M., Bevis, M., & Foster, J. (2000). January 30, 1997 eruptive event on kilauea volcano, hawaii, as monitored by continuous gps. *Geophysical Research Letters*, *27*(17), 2757–2760.

Papale, P., Neri, A., & Macedonio, G. (1998). The role of magma composition and water content in explosive eruptions: 1. conduit ascent dynamics. *Journal of Volcanology and Geothermal Research*, *87*(1-4), 75–93.

Pietruszka, A. J., & Garcia, M. O. (1999). The size and shape of kilauea volcano's summit magma storage reservoir: a geochemical probe. *Earth and Planetary Science Letters*, *167*(3-4), 311–320.

Poland, M. P., Miklius, A., & Montgomery-Brown, E. (2014). Magma supply, storage, and transport at shield-stage. *Charact. Hawaii. Volcanoes*, *179*(1801), 179–234.

Poland, M. P., Peltier, A., Bonforte, A., & Puglisi, G. (2017). The spectrum of persistent volcanic flank instability: A review and proposed framework based on kīlauea, piton de la fournaise, and etna. *Journal of Volcanology and Geothermal Research*, *339*, 63–80.

Pollard, D., & Delaney, P. (1978). Basaltic subvolcanic conduits near shiprock, new-mexico-dike propagation and dilation. In *Transactions-american geophysical union* (Vol. 59, pp. 1212–1213).

Reverso, T., Vandemeulebrouck, J., Jouanne, F., Pinel, V., Villemin, T., Sturkell, E., & Bascou, P. (2014). A two-magma chamber model as a source of deformation at grímsvötn volcano, iceland. *Journal of Geophysical Research: Solid Earth*, *119*(6), 4666–4683.

Ryan, M. P. (1988). The mechanics and three-dimensional internal structure of active magmatic systems: Kilauea volcano, hawaii. *Journal of Geophysical Research: Solid Earth*, *93*(B5), 4213–4248.

Segall, P., Anderson, K. R., Pulvirenti, F., Wang, T., & Johanson, I. (2020). Caldera collapse geometry revealed by near-field gps displacements at kīlauea volcano in 2018. *Geophysical Research Letters*, *47*(15), e2020GL088867.

Segall, P., Cervelli, P., Owen, S., Lisowski, M., & Miklius, A. (2001). Constraints on dike propagation from continuous gps measurements. *Journal of Geophysical Research: Solid Earth*, *106*(B9), 19301–19317.

Simons, M., Fialko, Y., & Rivera, L. (2002). Coseismic deformation from the 1999 m w 7.1 hector mine, california, earthquake as inferred from insar and gps observations. *Bulletin of the Seismological Society of America*, *92*(4), 1390–1402.

Tait, S., Jaupart, C., & Vergniolle, S. (1989). Pressure, gas content and eruption periodicity of a shallow, crystallising magma chamber. *Earth and Planetary Science Letters*, *92*(1), 107–123.

Tough, J., Blacknell, D., & Quegan, S. (1995). A statistical description of polarimetric and interferometric synthetic aperture radar data. *Proceedings of the Royal Society of London. Series A: Mathematical and Physical Sciences*, *449*(1937), 567–589.

Wilson, L., & Head III, J. W. (1981). Ascent and eruption of basaltic magma on the earth and moon. *Journal of Geophysical Research: Solid Earth*, *86*(B4), 2971–3001.

Yang, X.-M., Davis, P. M., & Dieterich, J. H. (1988). Deformation from inflation of a dipping finite prolate spheroid in an elastic half-space as a model for volcanic stressing. *Journal of Geophysical Research: Solid Earth*, *93*(B5), 4249–4257.

Zebker, H. A. (2017). User-friendly insar data products: Fast and simple timeseries processing. *IEEE Geoscience and Remote Sensing Letters*, *14*(11), 2122–2126.

Zheng, Y., & Zebker, H. A. (2017). Phase correction of single-look complex radar images for user-friendly efficient interferogram formation. *IEEE Journal of Selected Topics in Applied Earth Observations and Remote Sensing*, *10*(6), 2694–2701.